3D-Modelling and Investigation of the Lunar Exosphere: Light Noble Gases

LPE – BT 2023-12

Thesis for obtaining the degree

B.Sc.

at the School of Engineering and Design of the Technical University of Munich.

Advisor:	Alexander Smolka M.Sc.
	Professorship of Lunar and Planetary Exploration
Supervisor:	Prof. Dr.-Ing. Philipp Reiss
	Professorship of Lunar and Planetary Exploration
Submitted by:	Lenard James Dierksmeier
Place and Date:	Ottobrunn, 15.12.2023

Declaration of Academic Honesty

I declare that I will use all facilities, equipment, devices and programmes made available to me by TU München or by the Chair of Lunar and Planetary Exploration within the scope of my bachelor's, semester or master's thesis in accordance with the intended purpose, the valid guidelines, user regulations or instructions for use and, as far as necessary, only after having received instruction and with all due care. In particular, I will neither copy programmes without special instruction from the supervisor nor use them for purposes other than those intended for my work at the chair. I will not pass on to third parties any information, documents or findings that I have been told are confidential, either during or after my work at the Chair. I also agree that my bachelor's, semester or master's thesis may be made available by the Chair to interested persons upon request, also via a library, and that the results contained therein as well as developments and programmes resulting therefrom may be used by the Chair of Lunar and Planetary Exploration Technologies without restriction. Rights to any programmes and inventions that may arise must be clarified in advance. I also declare that I have prepared this thesis without outside help and have only used the sources and aids listed in the bibliography.

Ottobrunn, 15.12.2023

_____

Signature

Abstract

This thesis aims to develop a three-dimensional numerical model of the helium density of the lunar exosphere. A Monte Carlo simulation was used to achieve this and to simulate the ballistic trajectories of the particles hopping over the lunar surface. As the particle source, average solar wind conditions were assumed, and endogenic sources were not included in the model. For loss mechanisms of the neutral helium particles, gravitational escape and photoionization were considered. The model proved to be in accordance with reality since it remodelled the experimentally collected data by the LADEE space probe of the lower exospherical layers. The data showed that the helium particle density is much higher on the lunar nightside up to an altitude of about $750 \ \mathrm{km}$. Above, the fast and hot particles of the lunar dayside increase the density in these high exospheric layers on the dayside to values that cannot be reached in these high quantities by the cold and slow particles originating from the nightside. The density development was compared to the expected development assuming the barometric formula modified by *Chamberlain, 1963* for ballistically moving particles. The analysis showed that the Chamberlain formula can be applied to the nightside exosphere up to an altitude of $500 \ \mathrm{km}$. On the dayside the density decreased faster than expected using the Chamberlain formula, which was explained by mixing phenomena of particles with different temperatures.

Table of Content

List of Tables

List of Figures

Symbols & Constants

Symbol	Unit	Explanation	Value
A	m^2	Area	
AU	m	Astronomical Unit	$1.496 \times 10^{11} \,\mathrm{m}$
CV		Coefficient of variation	
E	J	Energy	
F	N	Force	
G	$\mathrm{m}^3\,\mathrm{kg}^{-1}\,\mathrm{s}^{-2}$	Gravitational constant	$6.673 \times 10^{-11}\,\mathrm{m}^3\,\mathrm{kg}^{-1}\,\mathrm{s}^{-2}$
H	m	Scale height	
h		Grid vector	
J	s	Area specific source rate	
j	$\mathrm{m}^{-2}\,\mathrm{s}^{-1}$	Particle flux	
k	s^{-1}	Photoionization rate	
k_B	$\mathrm{m}^2\,\mathrm{kg}\,\mathrm{s}^{-2}\,\mathrm{K}^{-1}$	Boltzmann constant	$1.380\,650 \times 10^{-23}\,\mathrm{m}^2\,\mathrm{kg}\,\mathrm{s}^{-2}\,\mathrm{K}^{-1}$
$m_{[atom]}$	u	Atomic mass	
m	kg	mass	
$N_{quantity}$		Number of a quantity	
n	m^{-3}	Particle number density	
P		Probability	
$\vec{r}$	m	Position vector	
r	m	Radius	
T	K	Temperature	
t	s	Time	
V	m^3	Volume	
v	$\mathrm{m}\,\mathrm{s}^{-1}$	Velocity	
X_i		Monte Carlo sample	
α		Thermal accommodation coefficient	
ϵ	J	Potential Energy	
ζ_{bal}		Partition function for ballistic movement	
θ	$^\circ$	Longitude	
ν		Photon	
σ	m^2	Photo cross section	
τ		Range of individual wavelength bins τ_i	
Φ	$\mathrm{m}^{-2}\,\mathrm{s}^{-1}$	Unattenuated solar photon flux	
φ	$^\circ$	Latitude	
φ_{co}	$^\circ$	Colatitude	
ψ	$^\circ$	Solar zenith angle	

List of Abbreviations

Abbreviation	Explanation
AU	Astronomical Unit
CDF	Cumulative Distribution Function
CV	Coefficient of Variation
ExESS	Extraterrestrial Exosphere and Surface Simulations
IID	Independent and Identically Distributed
LACE	Lunar Atmospheric Composition Experiment
LADEE	Lunar Atmosphere and Dust Environment Explorer
LT	Local Time
MC	Monte Carlo
NMS	Neutral Mass Spectrometer
PDF	Probability Distribution Function
SSE	Selenocentric Solar Ecliptic

1 Introduction

Our Moon has been a focused object of observation ever since humans started to look up into the sky. In the most recent times, our Moon became the object of the first unmanned exploration missions, and in 1969, with the Apollo 11 landing, even in the range for us humans. The following missions undertook a wide range of experiments, and the Apollo 17 mission found helium amongst other elements for the first time in the lunar atmosphere throughout the Lunar Atmosphere Composition Experiment (LACE)[1]. Since then, its origin has been investigated, and specific sources of helium have been evaluated. In 2013 and 2014, the Lunar Atmosphere and Dust Environment Explorer (LADEE) collected an extensive amount of data on the lunar exospheric particle densities that were used to evaluate several numerical models that were set up before to simulate the helium densities in the exosphere, one of them by *Grava et al.*, for example.[2]

The thesis aims to develop a three-dimensional model of the lunar exosphere, which allows us to predict the particle density of the noble gas helium at a given location in the lunar exosphere. The numerical model will be set up as a Monte Carlo simulation in which the trajectories of the helium particles are sampled, which perform ballistic hops over the lunar surface until they are eventually lost due to different implemented loss mechanisms.

The reader will first be introduced to the relevant fundamentals of exospheric physics used to develop the numerical model. This model will then be described concerning the structure of the Monte Carlo simulation, defining the in- and outputs and mentioning the necessary assumptions used to create the model. The statistical properties of the generated data are then investigated to verify the data's validity before analysing the grid elements' actual helium particle densities.

2 Fundamentals

2.1 The Moon

2.1.1 Earth-Moon Constellation

In a unique constellation in our solar system, the Moon is the natural satellite of our Earth. Its relative size compared to our planet is larger than that of every other moon-planet constellation in our solar system (only the moon of the dwarf planet Pluto is larger) and formed after a collision of the young Earth with a Mars-sized object. The radius is 1738 km, and the sidereal has a length of approximately 27.322 days. As displayed in Figure 2-1 below, the orbital plane of the Moon (on the right) surrounding the Earth (on the left) is inclined at $5.14°$ to the plane of the ecliptic and is therefore not aligned with the equatorial plane of our planet. The obliquity of the Moon relative to the ecliptic plane is $1.54°$ and very small compared to the Earth's obliquity of $23.44°$, which leads to very distinctly expressed seasons here on Earth.[3]–[5]
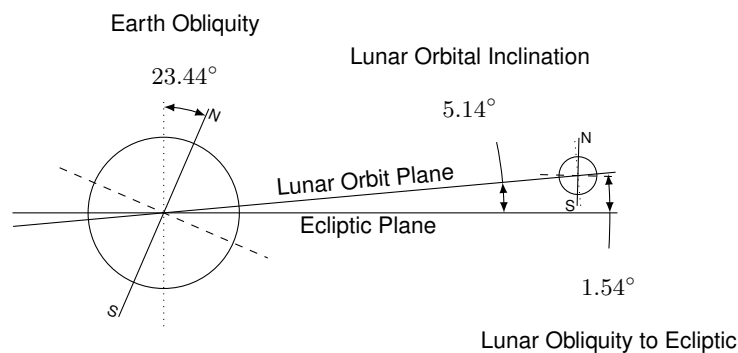
Figure 2-1 : *The figure shows the Earth and Moon in their ecliptic planes, with the inclination of their orbits displayed in between. Additionally, the obliquities of the Earth and Moon to the respective ecliptic plane are visualized. The figure was taken from Smolka, 2022.[5]*

2.1.2 Selenocentric Solar Ecliptic

The temperatures on the lunar surface strongly depend on the Sun's incoming radiation. Thus, it is essential to derive a coordinate system that describes the Moon's position dependent on the relative orientation to the Sun. The coordinate system used is the Selenocentric Solar Ecliptic (SSE) coordinate system. The x-axis of this system points to the Sun, the y-axis to the ecliptic north, and the z-axis completes the right-handed coordinate system. The SSE-longitudes can be then converted into local times (LT) by shifting the coordinate system by $180°$ with θ as the SSE-longitude:

$$LT = \frac{\theta - \pi}{\pi} \cdot 12\,hr. \tag{2-1}$$

This means, for example, that a SSE-longitude of $0°$ corresponds to a local time of $12\,hr$.[5]

2.2 Solar Wind

The ionized gas originating from the Sun is called the solar wind. It is mainly a mixture of predominantly protons and electrons. A small percentage comprises alpha particles and heavy ions in different ionization stages. The particle intensity of the solar wind decreases quadratically considering mass conservation law and the spherical geometry of the Sun.[6] Helium plays an important role in the dynamics of the solar wind and and the Sun's structure. Its abundance in the wind can change within minutes. Coronal mass ejection events can be very rich in helium, especially. Furthermore, the abundance of helium in the solar wind depends on the particle velocity and the time of the solar cycle. At low velocities of about 274 km s^{-1}, the helium abundance correlates well with the number of sunspots. However, in general, that dependency decreases with growing particle velocities. At about 560 km s^{-1} there is no visible correlation left.[7] Following *Grava, 2021*, the flux of alpha particles equals, on average, about $8 \times 10^6 \text{ cm}^{-2} \text{ s}^{-1}$ and makes up about 4% of the total particle flux of the solar wind [1].

2.3 Lunar Exosphere

The lunar exosphere is a specific type of exosphere, the so-called surface-bounded exosphere. The atmosphere is so tenuous that the particles do not collide or interact with each other. After being launched from the surface, they escape the gravitational field of the Moon, on the one hand, or fall back to the ground and are being relaunched, on the other hand. [5]
The LACE experiment, which deployed a mass spectrometer on the lunar surface during the Apollo 17 mission, first found helium, amongst other elements, in the lunar exosphere. With argon-40, it is the most abundant element in the exosphere with peaks of a few 10^4 cm^{-3} just after midnight local time. The primary source for these particles is the solar wind with its alpha particles. Secondly, there are endogenic particle sources such as the decay of ^{232}Th and ^{238}U within the lunar crust with about $1.49 \times 10^6 \text{ cm}^{-2} \text{ s}^{-1}$. The endogenic sources were found to make up about 19% of the total incoming particles, being consistent with the findings of the NMS instrument (Neutral Mass Spectrometer) on the LADEE space probe evaluated by *Benna, 2015* [2]. Following *Grava, 2021* the primary loss process is the gravitational escape with a 4.5 days escape time constant, which is the mean time a particle spends in the lunar atmosphere.[1]

The data collected by LADEE showed the abundance of the noble gases helium, neon and argon in the lunar exosphere. The probe detected the fluctuations of the noble gases in the atmosphere, which were found to be correlated to either solar particle events, which lead to a stronger solar wind, or the transit of the Earth's magnetic field, which shields the Moon from the solar wind. These findings support the thesis that the solar wind is the primary source of helium particles in the lunar exosphere.[2] After arriving on the lunar surface, the alpha particles are neutralized at the lunar regolith grains and then bounce in ballistic trajectories around the surface until they are lost to the surrounding space by gravitational escape or photoionization [1].

2.3.1 Lunar Surface Temperature

The surface temperature of the Moon is highly dependent on the amount of solar radiation reaching the lunar surface. For the desired model, it is critical to know the surface temperature at every point on the lunar surface to determine the initial particle velocities of the helium particles. The analytical function by *Hurley, 2015* and *Vasavada, 2012* offers a simple analytical model for the dayside with the solar zenith angle as the input only. The solar zenith angle ψ is the angle between the Moon-Sun line and the surface normal of the given point. At the terminator (the line on the surface separating the day- and nightside), ψ equals $90°$ The model for the nightside includes a dependency on the longitude θ and latitude φ of the point on the lunar surface. The analytical function for the dayside is provided by *Hurley, 2015* [8] as

$$T(\psi) = 262 \cos^{\frac{1}{2}}(\psi) + 130 \,\mathrm{K} \qquad \psi < 90°. \tag{2-2}$$

The solar zenith angle ψ is given as [9]

$$\psi = \cos\theta \cdot \cos\varphi. \tag{2-3}$$

The temperature of the nightside is given in dependency on the longitude θ and the colatitude $\phi_{co} = \frac{\pi}{2} - \varphi$). The longitude range is $\frac{\pi}{2} \le \theta \le \frac{3\pi}{2}$. The function is given as [8]

$$T(\theta, \varphi_{co}) = \sum_{n=0}^{5}(a_i\,\theta^i) + 35(\sin(\varphi_{co}) - 1) \qquad \psi > 90°, \tag{2-4}$$

with $a_i = [444.738, -448.937, 239.668, -63.8844, 8.34064, -0.423502]$.[8], [10] These functions lead to the maximum temperature of $392\,\mathrm{K}$ at the subsolar point ($12\,hr$ local time). The temperature falls to about 130 K post-sunset and 95 K before sunrise.[8] Figure 2-2 visualizes the analytical surface temperature function using a heatmap on the lunar surface. Higher temperatures are marked brighter and yellow, whereas cold temperatures are marked with dark blue. As expected, the highest temperatures occur at the subsolar point with about 400 K and a falling temperature moving to the borders of the Sun-lighted area. Moving further to the blue, colder areas, the temperature is dropping very fast to about 100 K. The white line inside the blue area is the 100 K line dividing the cold area into two zones. This division shows that the polar regions on the nightside are the coldest places, together with the regions just before sunrise in the whole range of latitudes.

2.3.2 Thermal Accommodation

The incoming alpha particles from the solar wind and the neutral helium particles of the lunar exosphere are thermally accommodated to the grains of the lunar regolith. The thermal accommodation can be described by the accommodation coefficient α:

$$\alpha = \frac{E_{out} - E_{in}}{E_T - E_{in}}. \tag{2-5}$$

E_{in} is the energy of the incoming helium particle, E_{out} the energy of the particle leaving the surface and E_T the ernergy of the particle in thermal equilibrium.
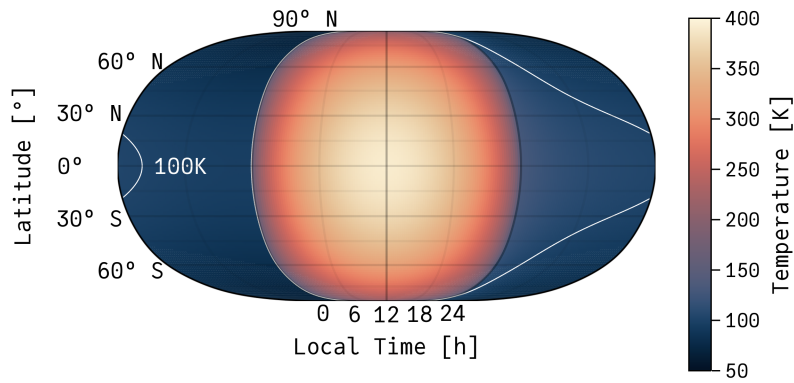
Figure 2-2 : The figure shows a heatmap of the lunar surface temperatures, an analytic function by Hurley et al.,2015. The temperature ranges from $50\,\mathrm{K}$ to $400\,\mathrm{K}$ with a corresponding colour scale from dark blue colours to bright yellow colours. It is visible that the highest temperatures are present at a latitude of $0°$ and a local time of $12\,hr$. The white line in the cold, dark blue area on the left and right indicates the $100\,\mathrm{K}$ line, making the temperature differences clear in the all-blue areas. It also shows that the coldest temperatures are present in the polar area on the nightside and just before sunrise. The figure was taken from Smolka, 2023.[9]

An accommodation factor of $\alpha = 1$ indicates an E_{out} that has the same value as E_T, and thus, the particle leaves the surface with no memory of its energy before the collision with the surface. *Grava, 2021* found that the exospheric helium can be described with full thermal accommodation ($\alpha = 1$) throughout the entire lunar surface.[1]

2.3.3 Photoionization

One of the mechanisms occurring in the lunar exosphere is the photodestruction of atoms and molecules, which means that the interaction with a photon destroys the specific particles. For the noble gases investigated here, a special form of photodestruction is becoming relevant: photoionization. The reaction is described as follows for the helium atom:

$$\nu + \mathrm{He} \longrightarrow \mathrm{He}^+ + \mathrm{e}^-. \tag{2-6}$$

The noble gas atom lost its neutral state with the ejected electron and will now be considered an ion.[9] The rate at which particles are ionized per second can be described by the rate coefficients k:

$$k_i(\lambda) = \int_{\lambda_i}^{\lambda_i + \Delta\lambda} \sigma(\lambda)\Phi(\lambda)\,d\lambda, \tag{2-7}$$

where $\sigma(\lambda)$ is the photo cross section of the specific atom and $\Phi(\lambda)$ is the unattenuated solar photon flux at wavelength λ.[11] These parameters are not known as continuous functions, so the approximation for each bin with a specific interval width of $\Delta\lambda$ of wavelengths is given with

$$k_i(\tau_i) = \sigma_i\Phi_i(\tau_i), \tag{2-8}$$

where σ_i is the wavelength-averaged photo cross section in the specific bin and $\Phi_i(\tau_i)$ is the unattenuated wavelength-integrated photon flux of that same bin τ_i.

Based on *Huebner, 1992* [11], the individual rates have to be summed over the whole range of bins τ, achieving a global photoionization rate k, with

$$k(\tau) = \sum_i k_i(\tau_i). \tag{2-9}$$

2.4   Mathematical Descriptions

2.4.1   Ballistic Flight in non-uniform Gravity

The helium particles perform very high ballistic jumps on the surface of the Moon. Thus, it is necessary to calculate the trajectories with non-uniform gravity. This approach leads to a differential equation of second order since the acceleration as the second derivative of the location is dependent on the location again. Using the gravitational law and Newton's second law,

$$\vec{F} = -G\,m_1\,m_2\,\frac{\vec{r}}{r^3} \qquad \text{and} \qquad F = m \cdot \ddot{\vec{r}}, \tag{2-10}$$

with the gravitational constant $G = 6.673 \times 10^{-11}\,\mathrm{m^3\,kg^{-1}\,s^{-2}}$, the gravitational force $\vec{F}$ on the particle, $m_{Moon} = 7.247673e22\mathrm{kg}$ as the mass of the Moon [9], $m_{He} = 4.002\mathrm{u}$ as the atomic mass of helium [9], $\vec{r}$ as the position vector of the helium particle (since the origin of the coordinate system is the centre of the Moon) and the absolute value of the position vector r, it is possible to calculate the gravitational acceleration at a given point in the lunar exosphere.[3]

Through combining the two equations, it is possible to find the following equation for the gravitational acceleration:

$$\ddot{\vec{r}} = -G\,m_{Moon}\,\frac{\vec{r}}{r^3}. \tag{2-11}$$

2.4.2   Barometric Scale Height

The changes in density of an isothermal atmosphere can be determined using the scale height H. It is the height where a specific parameter (here: density) decreases by a factor of $1/e$.[12] Using the barometric scale law that defines the scale height, the densities at different heights can be compared and analyzed. The desired result should be whether or not the lunar exosphere can be described using that law. It is stated as follows:

$$H = \frac{Gm_{He}m_{Moon}}{k_B T}, \tag{2-12}$$

with the gravitational constant G, the masses of a helium particle and the Moon, the temperature T and the Boltzmann constant $k_B = 1.380650e-23\mathrm{m^2\,kg\,s^{-2}\,K^{-1}}$.[5], [9], [13]

For projecting the particle densities from one height to another, the formula developed by *Chamberlain, 1963* [14] is used:

$$n = \tilde{n} \cdot \zeta_{bal} \cdot e^{\varepsilon - \tilde{\varepsilon}}, \tag{2-13}$$

with the particle number density n, the particle number density at a known position ñ, the corresponding potential energies ε and $\tilde{\varepsilon}$ and the partition function ζ_{bal} for the ballistic movement of the particles.[14]

2.4.3 Maxwell-Boltzmann-Flux Distribution

Since *Grava, 2021* found the helium in the lunar exosphere to be well described by the Maxwell-Boltzmann-Flux distribution with full thermal accommodation on the entire lunar surface (day- and nightside), this type of velocity distribution will be used in the simulation.[1] This means the energy of the leaving particles can be determined by knowing the temperature of the particular point the particle interacts with before performing its ballistic jump. After the first numerical simulations of exospheres with particle energies determined by the Maxwell-Boltzmann distribution it was found that this type of distribution would not produce an exosphere, which was in line with the barometric scale law. Therefore, the Maxwell-Boltzmann-Flux distribution, also known as the Armand Distribution, was then used for these types of simulations.[13]

The Maxwell-Boltzmann-Flux Distribution can be separated into its three components, which represent two lateral and one vertical component of the velocity vector:

$$P_3 = \underbrace{\left(\sqrt{\frac{\beta}{\pi}} \cdot e^{-\beta v_x^2}\right)}_{P_B(v_x)} \underbrace{\left(\sqrt{\frac{\beta}{\pi}} \cdot e^{-\beta v_y^2}\right)}_{P_B(v_y)} \underbrace{\left(2\beta v_z e^{-\beta v_z^2}\right)}_{P_A(v_z)}, \tag{2-14}$$

$$\beta = \frac{m}{2 k_B T}. \tag{2-15}$$

The two components in the x and y direction are derived from the Boltzmann distributions; the third part is the vertical velocity component. The temperature T is the temperature of the initial starting position. The formula shows there is a symmetry between the probability components of the two lateral components, which are equal. The following equation relates the third vertical component and the first two: $P_A = 2\sqrt{\beta \pi} \cdot v_z \cdot P_B$. This relation implies that the velocity in the vertical direction exceeds the velocities in the lateral directions on average. The equations above allow us to build the probability density function (PDF) for the three velocity components with a temperature-specific profile.[15] The model will use the already implemented Maxwell-Boltzmann-Flux distribution of the ExESS package.[9]

3 Model Description

This chapter will explain the development of the model as the foundation of this thesis. The model is implemented into a Monte Carlo simulation using the IID principle (independent particles, identically distributed) to simulate a specific number of particles to analyze their behaviour in the lunar exosphere and gain data about the densities of different exospheric altitudes. In this case, using the IID principle is possible since the definition of the exosphere specifies that the particles do not interact with each other, unlike the interaction in the much denser atmosphere of the Earth, for example.

3.1   Extraterrestrial Exosphere and Surface Simulations - ExESS Package

The ExESS package consists of tools and functions for the (as the name already suggests) simulation of exospheres and surface mechanisms of extraterrestrial places such as the Moon. The package supports the user with included physical constants and functions for calculating occurring mathematical and physical problems such as particle trajectories or surface temperatures. In detail, there are the following different categories of content:

1. Base,

2. Exospheres,

3. Grids,

4. Surfaces.

The used contents from the first container, "Base", include physical constants such as the lunar radius or the lunar mass, on the one hand, and practical functions for converting coordinate systems, spherical to cartesian coordinates/velocities, for example, on the other hand. One crucial part of the "Base" files is the Maxwell-Boltzmann-Flux distribution for sampling the particle start velocities. From the "Exospheres" container, the functions for calculating particle trajectories and generating time-dependent samples from those were used, as well as the tools to analyze the trajectory's properties, such as the landing position. From the "Grids" container, the structured 3D grid with equatorial symmetry and the functions to sort coordinate tripels to the grid were used. Of the functions the "Surfaces" container provides, only the temperature functions are relevant in this model.[9]

3.2   Monte Carlo Simulation

The Monte Carlo Simulation originated in the mid-1940s when the first computers were built, and scientists started to recognize the possibilities which came with it to simulate complex systems. Today, the Monte Carlo simulation is used in various areas, including physics, engineering, chemistry, and finance. The strength of Monte Carlo methods is the ability to simulate realistic systems that often include some randomness.

Statistical distributions can describe these randomly behaving variables in a variety of situations. In simulating the probabilistic acting systems, the randomly behaving variables are sampled from these distributions.[16]

The process of simulating a system can be stated based on *Lemieux, 2009* [16] as follows:

1. Choosing a suitable model for the process to be simulated with a description of the statistical distributions,

2. Implement the model in a computer program,

3. Receive several samples by running the code,

4. Gain statistical interference from the samples and decide if the simulation fits the reality.

This enumeration reflects the guideline on which the simulation was constructed. The following sections and chapters will show how the Monte Carlo simulation for analyzing lunar exosphere densities works, which conclusions can be drawn and if the data fits the real-life measured densities.

Figure 3-1 shows a schematic overview of a Monte Carlo simulation. It begins with initializing the global parameters used, e.g. physical values, variables or, as presented in the figure, the number of Monte Carlo steps N_{MC}, which is the number of iteration steps. The loop is then repeated N_{MC} times. The Monte Carlo step could contain several probabilistic and deterministic systems. The probabilistic systems sampled during the Monte Carlo step are usually the discussed distributions, for example, the Maxwell-Boltzmann-Flux distribution. The deterministic systems in this model are the analytically described trajectories of the particles, for example, that will be explained later in this chapter.

The single samples X_i are single realizations sampled from one or more probabilistic systems enclosed inside the Monte Carlo step. Each sample from a single iteration can also represent multiple realizations of the probabilistic systems if the Monte Carlo step is a collection of iteratively generated samples. An investigation of the statistical properties of the samples later has to take the number of single iterations per sample into account since, for example, the deviation between samples with a low number of single iterations is expected to be higher than between samples with a high number of iterations. The whole number of samples allows us to analyze the overall statistical properties of the simulated system.[9] The design of this closed system, which will be run through during the Monte Carlo step, is the first task of the list above and the focus of the following sections.

3.3   Model Assumptions

3.3.1   Setting

The desired model should deliver stationary data on the density of helium in the lunar exosphere at different heights. The Moon orbits the Earth and is rotating around its axis simultaneously.
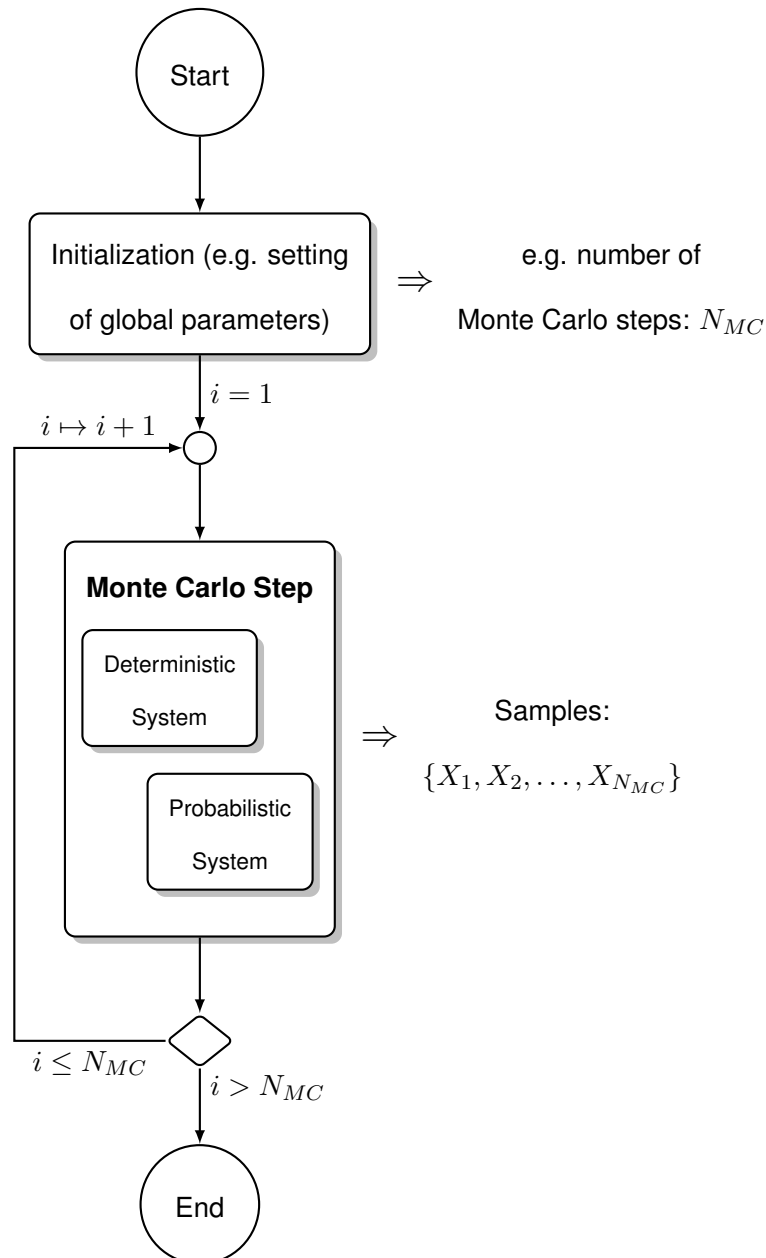
Figure 3-1 : *The figure shows a schematic overview of a Monte Carlo simulation, taken from Smolka,2023. The basic steps are visualized, keeping the Monte Carlo step generalized. The simulation starts with initializing the global parameters before handling those into the Monte Carlo step, where the probabilistic systems are sampled, and the data are further processed using the deterministic systems.[9]*

Due to the rotation around the Earth, sometimes the Moon moves through the solar shadow of our planet or lies within the influence of the Earth's magnetosphere. Since the solar wind consists of charged particles, the Moon is shielded from this particle source [3]. The rotation of the Moon around its axis makes it very difficult to use a fixed selenographic coordinate system since it would include rotating coordinates. The probability of a particle reaching the lunar surface (e.g. a solar wind particle) of a specific point would depend on the properties of the rotation. Not only does it make the model itself more challenging to set up, but it also increases the necessary computing power significantly and changes the problem from a stationary to an instationary problem. Instead, it is used a Sun-based global coordinate system defining local times as introduced in subsection 2.1.2.

Therefore, the (stationary) model will be built on the following assumptions regarding the setting:

1. The Moon is simulated to be at a distance of 1 AU from the Sun,

2. Any influence of the Earth is neglected,

3. The Moon itself does not rotate around its axis,

4. The Moon is modelled as a perfect sphere with a radius $r_{Moon} = 1737.4\text{km}$ [9].

3.3.2 Source and Loss Mechanisms

Different particle sources need to be evaluated for the simulation. The primary particle source is the solar wind described in section 2.2 with a flux $j_{solarwind} = 8 \times 10^{10}\text{m}^{-2}\,\text{s}^{-1}$ of alpha particles. Since the Sun is so far away from the Moon, the alpha particles originating from the Sun are assumed to move in trajectories parallel to the equatorial plane as presented in Figure 3-2 below:
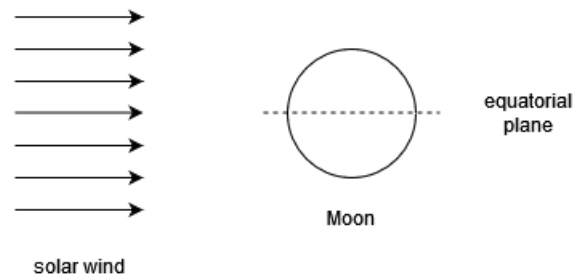
Figure 3-2 : *On the left, the solar wind trajectories are shown, which are assumed to be parallel since the Moon is so far away from the Sun. Additionally, they are assumed to be parallel to the equatorial plane of the Moon.*

The obvious determining factor for the total solar alpha particle flux is the projected surface of the Moon, which is rectangular to the direction of movement of the solar wind particles. Using the formula for the area of a circle, the total number of solar alpha particles reaching the lunar surface per second $J_{lunar-surface}$ calculates to:

$$J_{lunar-surface} = j_{solarwind} \cdot \pi r_{Moon}^2 \,, \tag{3-1}$$

with the particle flux of the solar wind $j_{solarwind}$ in $\text{m}^{-2}\,\text{s}^{-1}$ and the lunar radius r_{Moon} in meters.

Other particle sources are endogenic particle sources producing helium by radioactive decay. The endogenic sources were mentioned in the chapter 2 "Fundamentals" and release helium with a very static source rate. This source will be neglected.

Two loss mechanisms are considered in the model: gravitational escape and photoionization. The first one occurs when the kinetic energy of the particle is high enough to leave the gravitational field of the Moon.

The necessary escape velocity v_{esc} starting from the lunar surface can be written as follows:

$$v_{esc} = \sqrt{\frac{2G(m_{Moon} + m_{particle})}{r_{Moon}}} \,, \tag{3-2}$$

with the gravitational constant G, the lunar Mass M_{Moon}, the particle mass $m_{particle}$ and the lunar radius r_{Moon}. Since the particle mass is tiny compared to the lunar mass, the equation can be simplified to: [3]

$$v_{esc} = \sqrt{\frac{2Gm_{Moon}}{r_{Moon}}} \qquad m_{particle} << m_{Moon} \,. \tag{3-3}$$

The escape velocity from the lunar surface can be calculated that way to $2368 \,\mathrm{m\,s^{-1}}$.

The second loss mechanism already mentioned is photoionization. The phenomenon itself was already explained, the photoionization rates of helium during phases of a quiet Sun (normal Sun) are $0.525 \times 10^{-7}\mathrm{s^{-1}}$ and $1.510 \times 10^{-7}\mathrm{s^{-1}}$ for the active Sun.[11] The model uses the rates for the quiet Sun. Photoionization (as the name already states) only occurs in the presence of photons. Therefore, only particles exposed to sunlight can be ionized. Since the distance between the Sun and the Moon of 1 AU is high compared to the lunar radius, it can be assumed that the shadow of the Moon has the appearance of a tube rather than a cone, as presented in Figure 3-3 below.
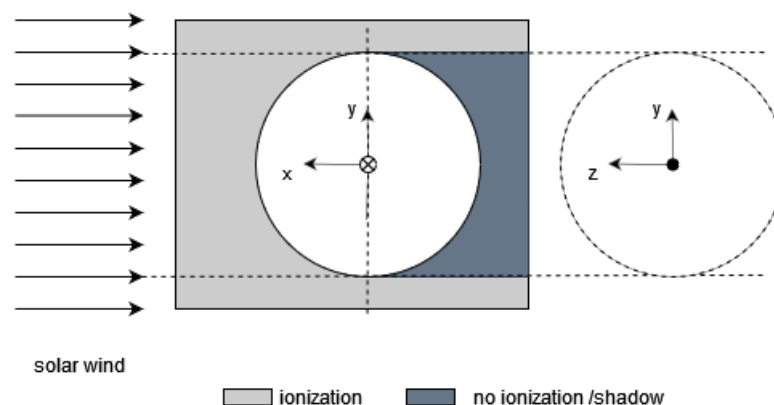
Figure 3-3 : *The approximation concept for the lunar shadow is presented for determining whether a particle is ionized. Since the Moon is far from the Sun, the solar wind particles are moving in parallel trajectories as introduced in Figure 3-2. The Moon in the centre creates a shadow displayed in the dark grey. In the light grey area, particles can be ionized. The SSE coordinate system for deciding whether ionization is possible is shown for the Moon and the tubular shadow's cross-section on the right.*

There must be a decision criterion to determine if a particle at a given position is exposed to sunlight. Looking at Figure 3-3, using the SSE coordinate system looks pretty comfortable like it is already displayed inside the Moon in the centre and for the tube's cross-section on the right. Suppose the current position of a particle on its trajectory has a positive x-coordinate, which is larger than the lunar radius, to be precise. In that case, there is always a chance to be ionized since it is constantly exposed to sunlight (the area where photoionization can occur is marked in light grey). If the particle has a negative x-coordinate, there must be a criterion if the particle's position lies within the tubular shadow (dark grey area) or outside of it and is exposed to sunlight again. The radius of the shadow is equal to the lunar radius r_{Moon} and the geometry of the tube is, as already implicated, circular, so the Pythagorean theorem can be used to determine permitted ranges of coordinates for the y- and z-axis to be inside the shadow. The condition can be formulated as follows:

$$r_{Moon} \geq y^2 + z^2 \ . \tag{3-4}$$

If the distance between the rotational axis of the tube and its outer boundary is smaller than the lunar radius, no photoionization can occur.

3.3.3   Assumptions on Particle Trajectories

The particles perform ballistic hops on the lunar surface as shown in Figure 3-4 below:
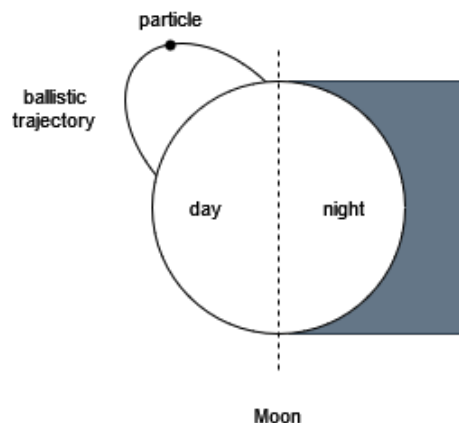
Figure 3-4 : The particle starts at a given location with a given velocity and performs a ballistic hop with a determined landing position that can be located both on the day- and nightside (dark grey colour). Additionally, it is possible that a particle exceeds the escape velocity and escapes the gravitational field; reaching an orbit around the Moo is impossible.

The particle starts on the lunar surface with a given velocity, which defines the reached height of the ballistic hop and, therefore, determines the landing position. Analytically, there has to be a landing position for a particle if it is not escaping the gravitational field of the Moon, which means reaching an orbit around the Moon is impossible.

The individual start velocity is sampled from the Maxwell-Boltzmann Flux distribution, where the likelihood of higher velocities grows with a higher surface temperature of the respective starting location on the lunar surface. The surface temperature will be gained from the function introduced in subsection 2.3.1. There will be full thermal accommodation used in the model just like *Grava, 2021* recommended (subsection 2.3.2). Forces between particles will be neglected. The only force acting on the particle after launching is the gravitational pull of the Moon, which will be assumed to be non-uniform and was introduced in subsection 2.4.1 to be: [3]

$$\ddot{\vec{r}} = -G\,m_1\,\frac{\vec{r}}{r^3}\,.$$

(3-5)

3.4   Model Preparations

Before implementing the developed model at the code level, it is necessary to define the inputs and the output for the reliable functionality of the model. Additionally, a numerical grid, serving as an auxiliary object, is used to categorize trajectory samples within its elements, thereby acquiring a critical role in ensuring the authenticity of the simulation. This section lays the groundwork by elucidating the specifics of these critical components, setting the stage for a robust and convincing model simulation.

3.4.1   Numerical Grid

The numerical grid used in this work's model is a 3D spherical grid which only spans the northern hemisphere of the Moon and uses equatorial symmetry to reduce the necessary number of elements and, therefore, save computing power. This approach assumes a symmetry between the northern and the southern hemispheres in which, for every particle changing its position between the hemispheres, another particle mirrors this behaviour in the opposite direction.[9] This approach is valid because the properties of the southern and northern hemispheres are assumed to be the same, and the simulation uses a number of simulated particles sufficiently high enough to neglect if a particle reaches a specific point on the northern hemisphere or the respective point on the southern hemisphere since another particle would always reach the same point on the other hemisphere. Figure 3-5 below defines this principle of building a hemisphere-spanning grid.
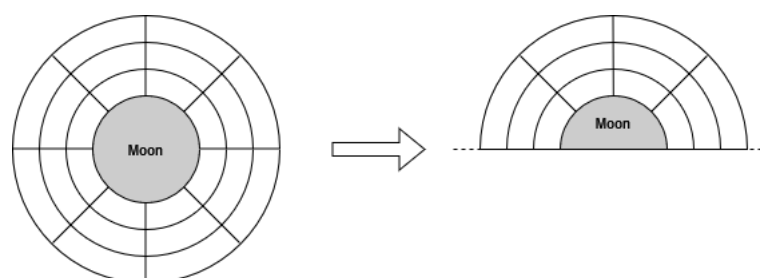

Figure 3-5 : *The reduction of a full spherical grid to a hemispherical grid*

The grid's properties include the radius of the body the grid uses as the base, the number of elements in longitudinal, latitudinal and radial direction, and every cell's coordinate in the global spherical coordinate system, surface areas and volumes.[9] The coordinates of each grid element are calculated using the following formulas, with the equation for the latitude adapted to the grid, which only spans the northern hemisphere (only defined for $\varphi \in [0, \pi/2]$):

$$\theta_i = -\pi + \frac{\pi}{N_\theta} + (i-1)\Delta\theta \qquad \text{for } i \in \{1, ...N_\theta\} \quad \text{with} \quad \Delta\theta = \frac{2\pi}{N_\theta} \, , \qquad (3\text{-}6)$$

$$\varphi_j = \frac{\pi}{4N_\varphi} + (j-1)\Delta\varphi \qquad \text{for } j \in \{1, ...N_\varphi\} \quad \text{with} \quad \Delta\varphi = \frac{\pi}{2N_\varphi} \, , \qquad (3\text{-}7)$$

with the longitudinal coordinate of the i-th element in the longitudinal direction θ_i and the corresponding coordinate in the latitudinal direction φ_j. Together with the radial coordinate r, which depends on the height of the layer over the lunar surface, the triple of coordinates is complete. The point in the spherical coordinate system is located in the centre of the lower boundary of the grid. [9]

For the simulation, the following grid parameters are used:

Table 3-1 : *Grid parameters used in the simulation*

Parameter	Value
Base radius r_0	r_{Moon}
Number of elements in longitudinal direction N_θ	180
Number of elements in latitudinal direction N_φ	45
Number of layers in the grid/length of vector h	16

To generate elements with the same angular size of $2°$ in longitudinal and latitudinal directions, the number of elements in the longitudinal direction has to be four times the number of elements in the latitudinal direction since the longitudes span the whole sphere and the latitudes are only defined for a hemisphere. The vector h containing the heights of the grid's layers over r_0 was decided to contain the heights of 16 different layers, which was decided based on the following consideration:

The particles gain their kinetic energy by thermally accommodating to the lunar surface. The amount is determined by the Maxwell-Boltzmann-Flux distribution. The lunar exosphere's scale height defined in chapter 2 "Fundamentals" provides an orientation. The scale height depends on the temperature of the atmosphere, which is believed to be isothermal and assumed to be the ground temperature. This assumption explains why the scale height of a column of the exosphere is higher on the Sun-lighted side than on the nightside. To underline this assumption with quantitative data, one can calculate the spread of the scale height between the hottest and the coldest point on the surface, which is the subsolar point, and a point just before sunrise as it was explained in subsection 2.3.1. This calculation leads to a scale height H of about 500 km in an exospheric column over the subsolar point and a scale height of about 120 km in a column over the coldest point.

An approximation is used to estimate the fraction of particles reaching the scale height: It will be assumed that the velocity components have the same amount on average. This approximation means one-third of the particle's kinetic energy flows into the z-direction for gaining height. It will also be assumed that only the z-component is responsible for gaining height (valid for a plane but with restricted validity for a sphere), which is valid for small trajectories of slow particles. The higher the particle energies, the more the two other components matter, so the estimation of the 1000 and 1500 km calculations is limited.

The velocity needed to reach the height of about $500 \mathrm{~km}$ can be determined by equating the kinetic energy E_{kin} (times one-third for this approximation) with the potential energy in non-uniform gravity E_{pot} in the non-vectorial 1D form (the only direction taken into account is the radial direction) and solving for the velocity:

$$E_{pot} = \int_{r_{Moon}}^{r_{Moon}+h} \frac{Gm_{Moon}m_{He}}{r^2} \, dr \qquad \text{and} \qquad E_{kin} = \frac{1}{3} \cdot \frac{1}{2} m_{He} v^2 \qquad (3\text{-}8)$$

$$\Rightarrow v = \sqrt{6 m_{Moon} G \cdot \int_{r_{Moon}}^{r_{Moon}+h} \frac{1}{r^2} \, dr} \, . \qquad (3\text{-}9)$$

After solving the integral with the lunar radius as the lower boundary and the lunar radius plus the height $h = H = 500 \mathrm{~km}$ the required velocity equals $1939.11 \mathrm{~m\,s^{-1}}$.

As already stated, the particles' start velocity is determined by sampling from the Maxwell-Boltzmann-Flux distribution. Figure 3-6 shows the PDF (Figure 3-6a) on the left and the CDF (Figure 3-6b) on the right (cumulative distribution function of the Maxwell-Boltzmann-Flux distribution). Displayed on the x-axis is the amount of the velocity vector sampled from the distribution in both diagrams. The corresponding probability to each velocity is on the y-axis in the PDF plot. The PDF and CDF are shown for the highest and the lowest temperature occurring on the lunar surface, with the hottest with $T = 392 \mathrm{~K}$ in the orange and the coldest one with $T = 95 \mathrm{~K}$ in the blue colour. The CDF shows the cumulated probability density on the y-axis, which is the area under the PDF upon the considered point. It is visible that the PDF of the lower temperature peaks earlier than the PDF of the higher temperature being $769 \mathrm{~m\,s^{-1}}$ for $T = 95 \mathrm{~K}$ and $1563 \mathrm{~m\,s^{-1}}$ for $T = 392 \mathrm{~K}$. This delta results from the strong dependency of the Maxwell-Boltzmann-Flux distribution on temperature. It leads to a CDF plot in which the cumulated probability density of the colder temperature rises much faster than the graph corresponding to the hotter temperature. The percentage of particles exceeding the height of $500 \mathrm{~km}$ can be determined using the CDF. The percentages with the corresponding height and temperature are displayed in table 3-2 below.

Table 3-2 : Percentages of particles not exceeding the height of $500 \mathrm{~km}$, $1000 \mathrm{~km}$ and $1500 \mathrm{~km}$ for the temperatures $T = 392 \mathrm{~K}$ and $T = 95 \mathrm{~K}$

Temperature	Height		
	500 km	1000 km	1500 km
$T = 392 \mathrm{~K}$	67.10%	88.90%	95.10%
$T = 95 \mathrm{~K}$	99.82%	99.90%	99.90%

(a) *PDF of the Maxwell-Boltzmann-Flux Distribution*　　　(b) *CDF of the Maxwell-Boltzmann-Flux Distribution*
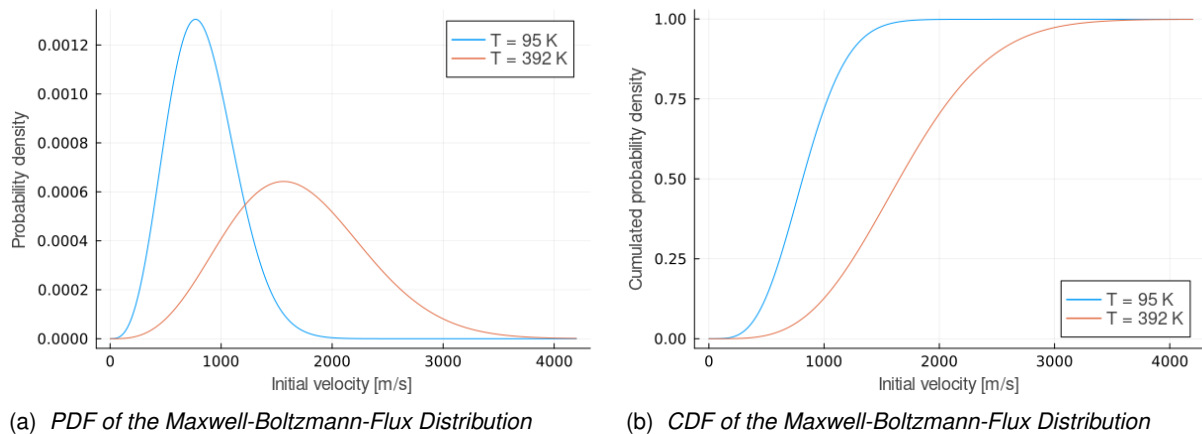
Figure 3-6 : The PDF and CDF of the Maxwell-Boltzmann-Flux Distribution shown for the two temperatures at the coldest point on the lunar surface with $T = 95\,\mathrm{K}$ in the blue colour and $T = 392\,\mathrm{K}$ in the orange colour for the hottest point. The x-axis in both plots contains the velocity, the y-axis in the PDF plot on the left contains the corresponding probabilities, whereas the y-axis in the CDF plot contains the cumulated probability density of the PDF.

The values inside the table show that almost 100% of the particles at the coldest point do not exceed the limit of $500\,\mathrm{km}$. At the hottest point, about two-thirds of the particles do not exceed the $500\,\mathrm{km}$ limit. To define a grid with equal heights for the day- and nightside, the first section of the grid until the height of $500\,\mathrm{km}$ was divided into ten subsections with equal hights of $50\,\mathrm{km}$. To prevent the grid elements higher than the first section from being empty, the second section up to a height of 1000 km was only divided into four subsections with an individual altitude of $125\,\mathrm{km}$ and the third section up to a height of 1500 km was divided into two subsections with an individual altitude of $250\,\mathrm{km}$. All particles above this limit are neglected and not considered in this model. Due to the numerical sampling and possible errors, all particles sampled closely beneath the surface are set to be in the radial distance of r_{Moon} to the lunar centre. The partition of the layer height vector h leads to a grid with $129\,600$ individual grid elements.

3.4.2   Input and Output

Defining the input and output variables is essential to a functioning model. The output is critical since the samples will be analyzed to gain knowledge about the simulated problem. The desired output of the density model should be a vector containing the data showing how often a particle was found in each cell. This vector will then be post-processed and statistically analyzed. The input variables are listed below in table 3-3.

3.5   Monte Carlo Step

The Monte Carlo Step is the heart of the simulation, in which the input variables are processed through the probabilistic and deterministic systems enclosed inside. The following section will outline the steps that were made and translated into the actual code sequences. Figure 3-7 shows the process sequence of the Monte Carlo step. Beginning at the starting node, visible in the figure, a new particle is initialized with its position and local velocity at a point on the lunar surface.

Table 3-3 : *Input parameters used in the simulation*

	Parameter		Value
1	Grid base radius	r_0	r_{Moon}
2	Number of elements in longitudinal direction	N_θ	180
3	Number of elements in latitudinal direction	N_φ	45
4	Vector containing layer heights	h	(specified above)
5	Grid portion height (1/3 of total)		$500 \, \mathrm{km}$
6	Time sample step	t_{step}	$15 \, \mathrm{s}$
7	Solar wind source rate	$j_{solarwind}$	$8 \times 10^{10} \, \mathrm{m^{-2} \, s^{-1}}$
8	Lunar radius	r_{Moon}	$1\,737\,400 \, \mathrm{m}$
9	Atomic mass helium	m_{He}	$4.002\,602 \, \mathrm{u}$
10	Photoionization rate helium	$\dot{s}_{He}$	$0.525 \times 10^{-7} \, \mathrm{s^{-1}}$
11	Monte Carlo steps	N_{MC}	(specified later)

The detailed procedure will be discussed in subsection 3.5.1. Then, it will be decided if the particle is lost with its initial velocity exceeding the escape velocity of the Moon (v_{esc}). If this is true, a new particle is initialized, and if the number of the simulated particles already equals the number of predefined Monte Carlo steps N_{MC}, the loop is terminated. If the velocity is less than v_{esc}, the particle's trajectory is calculated through numerical methods implemented in the ExESS package. Then, the trajectory is analyzed for every time step of $15 \, \mathrm{s}$ and the position data are extracted. A decision step follows this process, determining whether photoionization happens or not based on the photoionization rate of helium. If so, the position at which the particle is ionized, and all following positions of that specific trajectory are omitted. For the remaining positions (or all positions if the particle is not ionized), the corresponding grid element is then calculated, and a counter for each grid element is increased by the number of particles belonging to it. Finally, the landing point of the particle is set as the new initial position, and its new start velocity, depending on the temperature of this position, shall be determined. Thus, the number of sample trajectories does not have to equal the number of Monte Carlo steps.

3.5.1 Initial Position and Velocity

As explained before, the sequence of simulating each particle begins with identifying the initial position and, based on the result, its initial velocity. Figure 3-8 shows that there are two sources of initial positions for particles in this model: The first one is a new particle with a randomly generated position, and the second one is the landing position of an existing particle. The temperature is then calculated using the analytical function described by *Hurley, 2015* and *Vasavada, 2012* introduced in subsection 2.3.1. The temperature is then used to sample the initial velocity vector from the Maxwell-Boltzmann-Flux distribution implemented in the ExESS package.

Generating random positions on the lunar surface shall be done using the method of inverting a probability distribution. The idea is to generate samples from a given probability distribution by evaluating the corresponding inverse CDF using a uniform distribution between zero and one.[16]
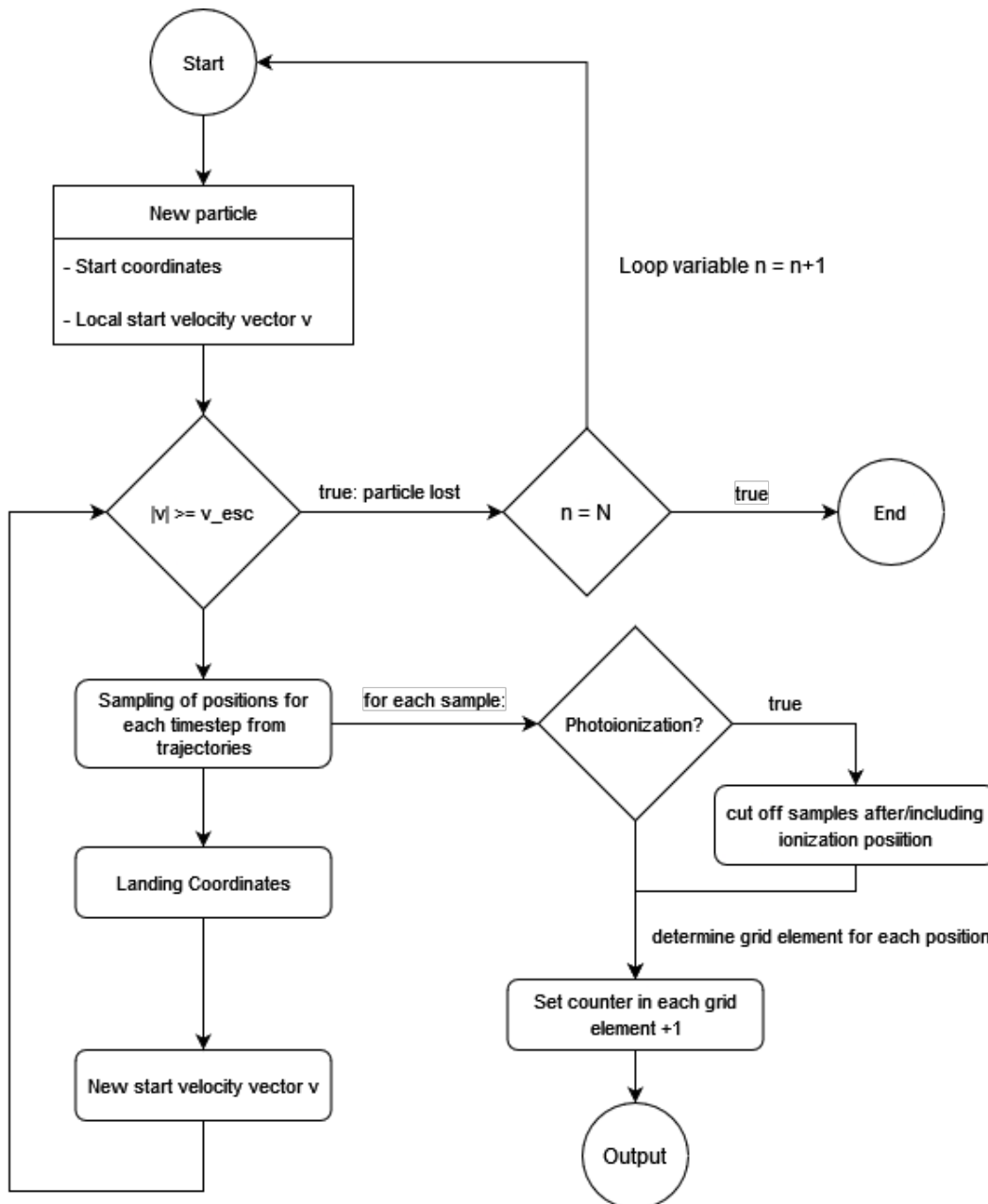
Figure 3-7 : *The diagram shows the Monte Carlo step of the density model, which was translated into the actual code sequence. After a new particle is initialized with its location and velocity, it is evaluated if the velocity exceeds the escape velocity of the Moon. If this is true, a new particle will be initialized; if not, the sequence continues by calculating the expected trajectory and sampling the positions for the defined time step. After that, the landing position is determined, and the sequence restarts with this new starting location. The sampled positions taken from the trajectory are evaluated if photoionization occurs; if this is true, this position and all following positions from that trajectory are omitted. The remaining positions are then sorted into the grid, where a counter in each element is increased by the number of particles found to be in this specific element.*

The particle source in this model is the solar wind, so the probability of a particle being generated on the nightside of the Moon equals zero. The number of particles per projected area reaching the surface near the equator is higher than near the poles since the projected area in the plane rectangular to the incoming solar wind is higher for an infinitesimal element at the equator than at the poles. The projected area is dependent on the cosine of the longitude θ and the latitude φ (at the subsolar point, the probability equals one, and the projected area approaches zero for $\theta = \varphi = 0°$).
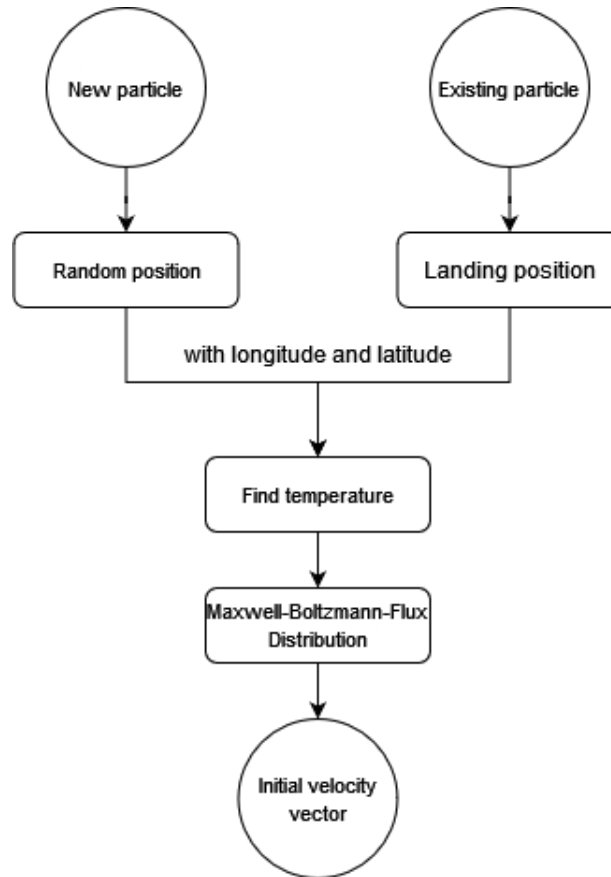
Figure 3-8 : *The process of finding a particle's initial position and deriving its initial velocity. Either the position is randomly generated on the dayside or an existing particle's landing position is used. Then, the temperature of this location is used to sample the velocity from the Maxwell-Boltzmann-Flux distribution.*

The longitude and latitude probabilities can be treated separately to generate the random position since they do not influence each other. Determining a point can be seen as a two-stage sampling. For a proper PDF, the probabilities have to be normalized, which will be done using the following condition: The CDF of the PDF times an unknown normalization constant A equals 1:

$$\frac{1}{A} \cdot \int_{-\frac{\pi}{2}}^{\frac{\pi}{2}} \cos\theta \, d\theta \stackrel{!}{=} 1 \, . \tag{3-10}$$

This equation can be written for θ and the same for φ. Solving it for A delivers the normalization factor $A = \frac{1}{2}$ in both cases. This means the normalized PDF function can be written as $\frac{1}{2}\cos\theta$ where θ is interchangeable with φ. Integrating the PDF for the CDF delivers the CDF function, in which the values lie between 0 and 1 per definition of a CDF function. Therefore, it is then equated with a realization of the uniform distribution r:

$$\int_{-\frac{\pi}{2}}^{\theta} \cos\theta \, d\theta = \frac{1}{2}(\sin\theta + 1) \stackrel{!}{=} r \qquad r \in [0, 1] \, . \tag{3-11}$$

This equation can then be transformed into the inverse CDF and the following equation:

$$\theta = \arcsin\left(2 \cdot r - 1\right) \, . \tag{3-12}$$

This equation gives a distribution of the longitude θ that is the same for the latitude φ based on the uniform distribution in the interval $[0, 1]$. This procedure can be easily implemented into the code.

3.5.2 Sampling Trajectories

After the particle's initial position and initial velocity are found, it is evaluated if the velocity exceeds the escape velocity. After that, the trajectory is calculated using the Runge-Kutta procedure. This step is implemented in the ExESS package. The trajectory is then sampled every 15 s, and the corresponding position is saved in a vector. Every position in this vector is then checked for whether photoionization can happen (if it is exposed to sunlight). If so, a random number between 0 and 1 is generated from a uniform distribution and compared to the photoionization rate times the time sample step of 15 s since the photoionization rate is given in s^{-1}. If the random number is larger than the calculated 15 second rate, the particle survives, and the next position is checked. If photoionization occurs, the corresponding position and all following positions on the trajectory are omitted in the next step, sorting the respective positions into the grid. If a position exceeds the maximum height of 1500 km, it shall not be part of the calculations here. For every particle sample inside a grid element, the counter for this element is increased by one. After this step, the particle's landing position is the new initial position for the subsequent trajectory. The same particle is iteratively simulated until it is lost by gravitational escape or photoionization.

4 Data Preparation and Verification

Before analyzing the data and drawing conclusions about the density model, the data's validity and value must be reviewed. The following chapter emphasizes the statistical validity of the data, examining if the number of Monte Carlo steps has led to convergence, indicating a reliable value for the later analysis. On the other hand, the value of the data regarding real-life conditions has to be examined. Good simulation data that do not comply with the real-life conditions in the lunar exosphere would not be meaningful in this context. The data will be compared to the data collected by the LADEE space probe and analyzed by *Benna, 2015* [2].

4.1   Statistical Verification

The data generated through the simulation will later be processed to be analyzed further and used to gain knowledge on the helium density of the lunar atmosphere. Beforehand, it has to be proven that the data are meaningful in their composition. A Monte Carlo simulation is driven by the goal to approximate the reality by evaluating the different realizations of the underlying probabilistic distributions until it nearly describes the reality. This section will prove the generated data's meaningfulness by showing the convergence of the Monte Carlo simulation.

The data were generated partitioned in 1000 files, each containing the data of $10\,000$ particles. The partitioning was done to compare the data amongst each other and find the necessary number of particle samples to generate a valid database. The first analysis would determine each grid element's standard deviation of counted particles. For better comparability between the day and nightside, which can have very different densities, the coefficient of variation (CV) is used, which is equivalent to the standard deviation being normalized using the mean of the counted particles of each element. The sample size for this statistical analysis is 1000 different data points for each element. The results are shown in the following figures.

Figure 4-1 shows the CV of the elements of the grid layers ranging from 0 to 50 km height on the left and from 875 to 1000 km on the right. The scales are the same for better comparability, beginning at zero and ranging up to 0.52. Dark blue indicates low coefficients, whereas bright yellow indicates high ones. The x-axis shows the local time on the surface, and the y-axis shows the latitude in degrees. The left figure (4-1a) shows that the variation coefficients are rather low in the first layer, indicated by blue colours. Different tones of blue indicate a difference between the day- and nightside (dayside is between 6 and 18 hr local time). The variation coefficient on the dayside is slightly higher and reaches values of about 0.1. This observation can be explained by the higher start velocities on the dayside due to the higher surface temperature. There is a higher variability in the start velocities, as shown in Figure 3-6. The elements in the polar region all show blue to red colours, indicating slightly higher coefficients than in the other parts of the map. The figure on the right shows the CV for the densities in the fourteenth layer between 875 and 1000 km. The map's colours changed compared to the left to blue-red, indicating coefficients of about 0.2.

(a) *Coefficient of variation of densities* 0 - $50\,\mathrm{km}$

(b) *Coefficients of variation of densities* 875 - $1000\,\mathrm{km}$
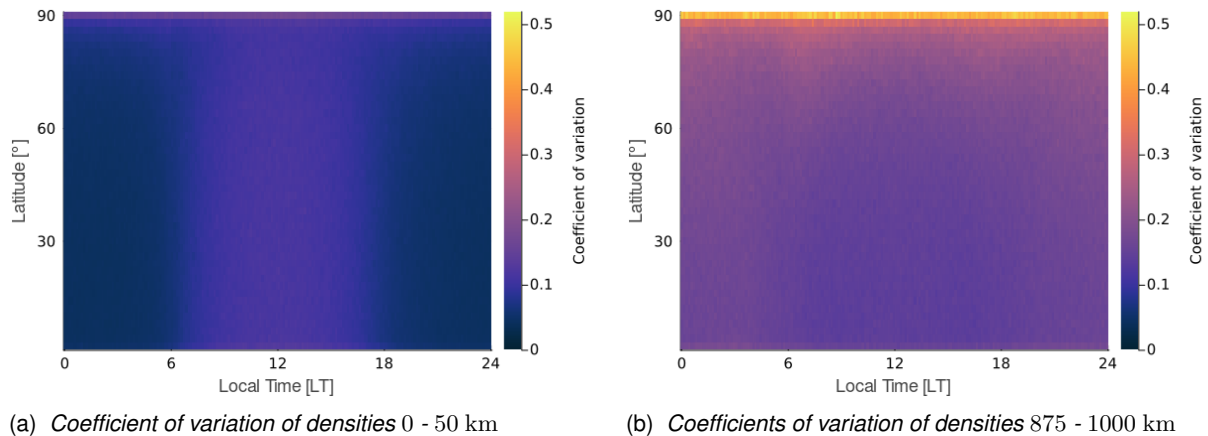
Figure 4-1 : The figures show the coefficients of variation of the density samples in the first layer of the grid ranging from 0 to $50\,\mathrm{km}$ on the left and between 875 to $1000\,\mathrm{km}$ on the right. The x-axis displays the local time, the y-axis the latitude and the colour axis ranges from dark blue to bright yellow, indicating growing values of the coefficient of variation. The scale ranges from 0 to 0.52. On the left side, the coefficient of variation is slightly higher on the dayside (about 0.1, indicated by a lighter blue). The polar elements of the heatmap show a coefficient of variation between 0.2 and 0.3, indicated by a slight red. The polar regions on the right show a bright yellow, indicating a coefficient of variation of about 0.5. In this height of about $1000\,\mathrm{km}$, the night side and the dayside regions of high latitude over $60°$ show a slight red, whereas the dayside regions lower than $60°$ of latitude are more blue indicating lower coefficients of variation.

When moving up to the polar regions, the colours shift to red before the polar elements appear in a bright yellow, indicating values of about 0.5. The colour shift means the CV is growing faster there than everywhere else. This effect can be derived from smaller grid element sizes of polar regions. There are 180 elements spanning the hemisphere in the longitudinal direction that span the lunar circumference in the equator region but only span a fraction of that in the polar regions. Therefore, the probability increases that an element is not sampled in a polar element even if it crosses it. In the area of local times between 6 and $18\,hr$ and latitudes up to $60°$, it is visible that the CV is smaller there than in higher latitudes on the dayside and the nightside. It can be explained by the number of particles that reach these heights on the dayside due to the high surface temperature, especially in these latitudes. On the nightside and in high latitudes, only single particles are sampled in these grid elements.

The described phenomena occurring in lower heights on the dayside with a higher CV changing to the dayside having a lower CV in low to mid-latitudes is emphasized in Figure 4-2 below with the first layer between 0 and $50\,\mathrm{km}$ shown on the left and the highest layer of the grid ranging from 1250 to $1500\,\mathrm{km}$ over the lunar surface shown on the right. The colour scales have been optimized for clear visualization, ranging from 0 to 0.2 on the left and from 0.15 to 0.35 on the right. Figure 4-2a shows the difference between day- and nightside much better than the figures above that have been used for global comparison. The red colours on the dayside turn sharply into blue at the lunar sunrise terminator at $6\,hr$ local time and $18\,hr$ at the lunar sunset terminator. The polar elements appear in bright yellow now, indicating their higher CV. Beginning at a latitude of about $80°$, it is visible that the visibly bordered dayside area fans out to the whole width of the local time. In this area, the effects of the decreasing size of the elements become visible. The figure on the right shows the most extreme reversion of the conditions in the lower layers with a visible lower CV on the dayside at low-mid latitudes introduced by describing Figure 4-1.

These areas appear dark blue, indicating low CVs of about 0.15. In contrast, the nightside and higher latitudes on the dayside appear in a lighter blue, indicating coefficients of about 0.185 before shifting to red and then to yellow in the polar regions.


(a) *Coefficients of variation of densities 0 - $50\,\mathrm{km}$*

(b) *Coefficients of variation of densities 1250 - $1500\,\mathrm{km}$*
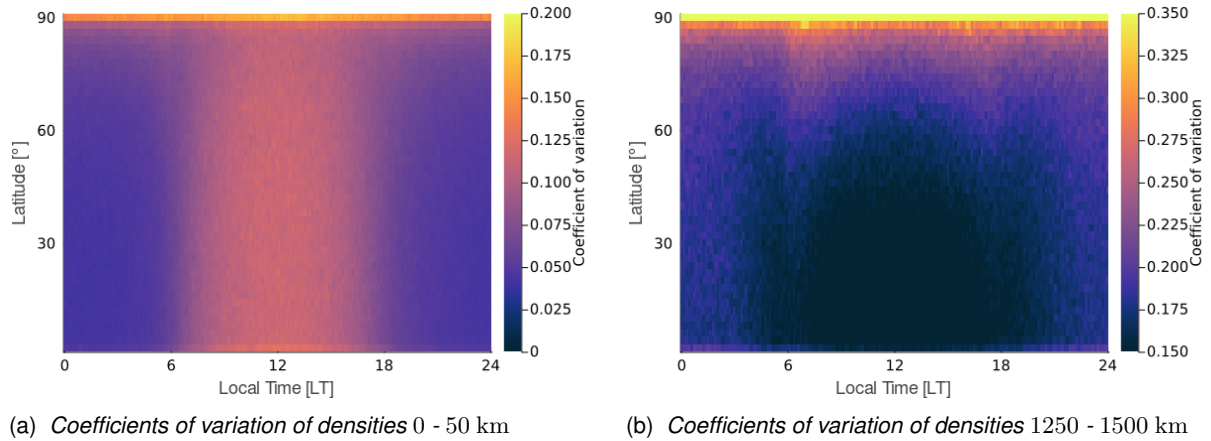
Figure 4-2 : The coefficients of variation of the densities are displayed in 0 to $50\,\mathrm{km}$ height on the left and in 1250 to 1500 km height on the right. The scale of each figure was optimized to emphasize the respective effect to be shown. The coefficients of variation are graded on the colour scale from a dark blue to a bright yellow and are plotted over the x-axis, indicating the local time on the surface and the latitude on the y-axis. The figure on the left shows the distinct difference of the coefficients of variation between day- and nightside fanning-out to the whole width at latitudes of about $80°$. The figure on the right shows that the conditions are reversed in higher layers. The region with lower coefficients of variation is now the dayside in low to medium latitudes. This difference occurs because of the higher start velocities on the dayside.

For a better overview of the development of the CV, Figure 4-3 shows its development compared between the layers. The CVs of each layer are normalized with the layer volume of the respective layer. Therefore, the polar elements, smaller in volume than the equatorial elements, with their high CVs, are weighted less. The calculation is done using the following formula:

$$CV_{L,V,norm} \;=\; \frac{CV_E \cdot V_E}{V_L} \qquad \text{and} \qquad V_L \;=\; \frac{4}{3} \cdot \pi \cdot (r_{L,upper} - r_{L,lower})^3 \,, \qquad (4\text{-}1)$$

where $CV_{L,V,norm}$ is the CV normalized with the respective layer volume V_L, CV_E is the CV and V_E the volume of the respective element. $r_{L,upper}$ and $r_{L,lower}$ are the radii of the upper layer boundary and the lower layer boundary. Listed on the x-axis is the number of Monte Carlo steps in 1×10^4 steps, and on the y-axis, the value of the layer volume normalized coefficients of variation. The light blue line represents the mean value of all normalized coefficients of variation of the density data of a layer, the dark blue dashed line the standard deviation of the dataset and the ribbon marks the maximum and minimum values. The mean value generally increases, reaching higher layers with two prominent exceptions at $x = 10$ and $x = 14$. After these points, the mean value decreases until it grows again when it reaches the next layer, which can be explained by the increasing height at these points. After 10 layers the layer height increases from $50\,\mathrm{km}$ to $125\,\mathrm{km}$ and after 14 layers it increases to $250\,\mathrm{km}$. Therefore, more particles will be sampled in these elements as they combine many cells to a bigger volume.

Generally, the volume normalized values behave very statically, with a small growth in the range of the maximum and minimum values moving to higher layers. This effect can be explained by the generally higher CVs in the higher layers, as observed in Figure 4-2. The development of the mean value is mirrored by the development of the maximum values without any larger breakouts, which indicates that there are no zones on the exosphere where the deviations from the mean are significantly higher than elsewhere. Additionally, the standard devation shows, that the majority of the values is focussed in a thinner band than the blue filled area around the mean. Therefore, the significance of the deviation of the minimum and maximum values is limited.
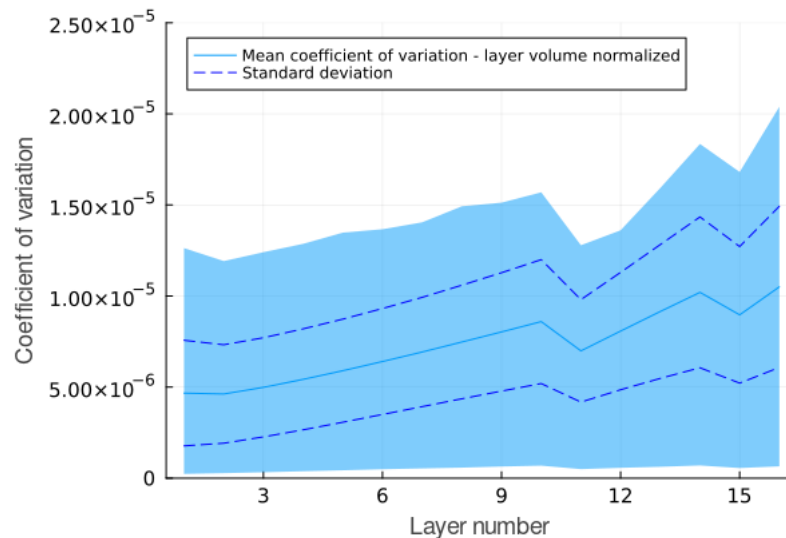

Figure 4-3 : *The layerwise development of the coefficients of variation of the density values normalized with the respective layer volumes is shown. The blue line is the mean value of these normalized coefficients of variation showing, in general, an increase except for $x = 10$ and $x = 14$ where the layer height is increased and thus the coefficients of variation decrease since more elements are combined to a larger one. The dark blue dashed line represents the standard deviation of the dataset and the filled blue region marks the span between the extreme values of the coefficients of variation of each layer.*

Generally, the CVs are relatively small and of small acceptable values, indicating low deviations in the data, and they show beneficial statistical properties for further analysis.

The last property of the data set which needs to be investigated is if the Monte Carlo simulation shows convergence. That was done by comparing the 1000 different samples generated by the simulation containing each $10\,000$ trajectories. The CV is calculated using the density data in the different samples for each element. Then, from all variation coefficients, the standard deviation is calculated. It is then used to assess the accuracy of the simulation.

Figure 4-4 shows the development of the standard deviation of the CVs displayed on the y-axis for the number of files used for the comparison displayed on the x-axis. It is visible that the standard deviation is falling sharply within the first 100×10^4 steps and shows no more visible changes after 250×10^4 steps. For this plot, the coefficients of variation are normalized with the total grid volume to adjust the weighting between the larger and smaller volumes of the elements using the following equation:
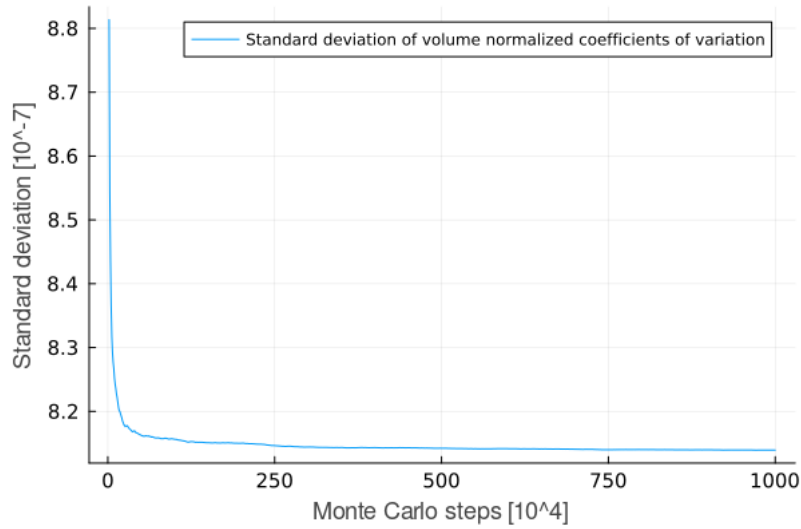
Figure 4-4 : The graph describes the correlation between the standard deviation of the coefficients of variation of each grid element displayed on the y-axis and the number of Monte Carlo steps displayed on the x-axis. It is visible that the standard deviation is falling sharply within the first 100×10^4 steps and then shows no more change after 250×10^4 steps. That means the simulation shows convergence for the models' number of Monte Carlo steps.

$$CV_{G,V,norm} = \frac{CV_E \cdot V_E}{V_G} \qquad \text{and} \qquad V_G = \frac{4}{3} \cdot \pi \cdot (r_{G,upper} - r_{G,lower})^3 \,, \qquad (4\text{-}2)$$

where $CV_{G,V,norm}$ is the CV normalized with the respective grid volume V_G, CV_E is the CV and V_E the volume of the respective element. $r_{G,upper}$ and $r_{G,lower}$ are the radii of the upper and lower grid boundary. The standard deviation combining all files equals 8.13×10^{-7}, a minimal value indicating excellent simulation accuracy.

4.2   Data Preparation

The data generated by the Code based on the model developed in chapter 3 still need to be processed to be comparable to real-world densities. The output vector contains the counted number of sampled particles inside the cell referred to by the index of the vector's element. This number is directly dependent on the number of Monte Carlo steps as it generally grows with more particles sampled. Therefore, different post-processing has to be applied to the output data. The two numerical properties influencing the data are the trajectory sampling timestep, and the Monte Carlo steps. The timestep was set to 15 s and the number of Monte Carlo steps to 1×10^7. The simulation particle counter numbers have first to be normalized by the number of Monte Carlo steps leading to an encounter-probability of sampling a particle in an element when simulating one particle in total:

$$P_{encounter} = \frac{N_{counter}}{N_{MC}} \qquad (4\text{-}3)$$

with the encounter-probability $P_{encounter}$, the counted particles in each grid element $N_{counter}$ and the Monte Carlo steps N_{MC}. The timestep t is part of the weighting of the simulated particles.

Since the simulated numbers per element must be transformed into real particle densities per volume, the source rate per second becomes an important influencing factor. Its unit is particles per area and second that reach the lunar surface. The time dependency has to be eliminated here. Therefore, it is assumed that the simulated state is stationary and time-invariant. This means that many particles are moving in the same direction on each trajectory. It is now assumed that all simulated particles started at the same time. Their position is then sampled every 15 s, which means that in the time interval before the first position is determined 14, more particles start their trajectories. Combining this assumption with the first one that these 14 particles are moving on the very same trajectory, they are simulated in combination, which gives each simulated particle a weighting of 15. The real number of particles which should be found in each element is then determined using the weighting and the source rate introduced in section 2.2. The area which needs to be taken into account for the number of particles reaching the lunar surface every second is determined using the projected area of the Moon in the direction of the solar wind, which is the area of a circle with the same radius as the Moon $A_{proj} = \pi r_{Moon}^2$. The actual number of particles in each element is then found using the following equation:

$$N_{real} = P_{encounter} \cdot j_{solarwind} \cdot A_{proj} \cdot t_{step} \tag{4-4}$$

with the actual number of particles per element under the assumed conditions N_{real}, the encounter-probability $P_{encounter}$, the solar wind source rate $j_{solarwind}$, the projected area A_{proj} and the time step t_{step}.

The data must be connected to each element's volume to gain particular particle number densities per volume from these data. The equation for the desired data format of particular particle numbers per volume leads to the following final equation:

$$n = \frac{N_{real}}{V_E} \tag{4-5}$$

with the particle number density $n \text{ particles/m}^3$ and the volume of the specific grid element $V_E \text{ m}^3$. This way, the gained data can be further analyzed regarding validity compared to collected data and simulations that fit the real data.

4.3   Data Verification

Additionally, for further analysis and to conclude the data, it is necessary to compare the data generated by this model to reliable data sources and validate the generated model data. The main comparison data used in this verification are the LADEE NMS data investigated by *Benna, 2015*, introduced in section 2.3. LADEE covered a $\pm 23°$ equatorial band with its measurements ranging from 4 km to 60 km over the lunar surface. The data show a peak at $6.5 \times 10^4 \text{ cm}^{-3}$ of the helium density $20°$ past the lunar midnight meridian, which corresponds with a longitude of $200°$ beginning at the lunar subsolar meridian as displayed in Figure 4-5b.

The ratio of the maximum density on the nightside and the minimum density on the dayside was determined by *Benna, 2015* to be 28, which equals a minimum surface density of 2.32×10^3 cm^{-3}.[2] The LADEE helium density data plotted over the longitude beginning at the subsolar meridian show an almost symmetric behaviour, with the maximum being slightly shifted past the lunar midnight meridian, as stated before. Therefore, the decrease in the density after the peak is slightly sharper than the increase in front of the peak. Figure 4-5 compares the LADEE data on the right to the model-generated data on the left. The source elements of the grid are located in the same equatorial band ($\pm 24°$) as the LADEE data and are taken from the grids' first layer ranging from the lunar surface to an altitude of 50 km, covering almost the entire LADEE measurement layer which provides good comparability. The data were multiplied with the factor of 2.5 determined by *Benna, 2015* to compare the model data based on average source rates to the LADEE data, which show the influence of solar particle events leading to higher density values. Additionally, the missing contribution of the endogenic sources was added to the densities.


(a) *Surface densities projected down from 25 and 50 km*

(b) *Surface density as observed by LADEE taken from Benna, 2015 [2]*
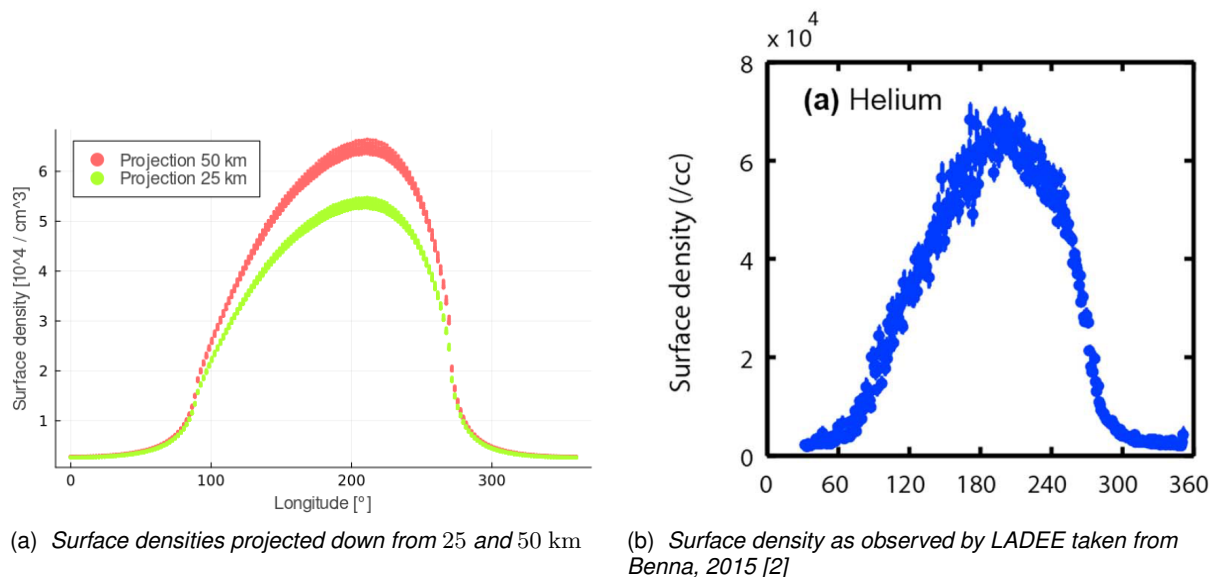
Figure 4-5 : In the right figure, the helium density data collected by the LADEE space probe are plotted on the y-axis over the longitude beginning at the subsolar meridian on the x-axis. The density increases with the increasing longitude and peaks at $200°$, $20°$ past the lunar midnight meridian with the density of $6.5 \times 10^4 \text{ cm}^{-3}$. After the maximum, the density decreases in an almost identical manner, only slightly faster, as it rose before. At about $300°$, a small curvature is more formed out, compared to the respective section on the other side of the peak. On the left side, the respective data generated by this thesis's model are plotted for the same longitudes on the x-axis and with the density on the y-axis. The data used for this diagram were taken from the elements of the grid (an equatorial band with $\pm 24°$) that form the same equatorial band which LADEE covered during its measurements and from the first layer of the grid ranging from the lunar surface to an altitude of 50 km, covering almost the entire LADEE measurement layer ranging from 4 km to 60 km. For the red graph, the density data were projected down to find the surface density from the top of the first layer, and for the green graph, from half of the height of the first layer. It is visible that the red graph represents the LADEE data better as its maximum density equals $6.64 \times 10^4 \text{ cm}^{-3}$, compared to $5.48 \times 10^4 \text{ cm}^{-3}$ for the green data. The longitude for the peaking density equals $31°$ past the lunar midnight meridian for the red data and $29°$ for the green data.

For the red data, the density was projected down using the formula developed by *Chamberlain, 1963* from the top of the first layer and for the green data from half of the layer height of the first layer.[14] Both plots share the characteristics of the LADEE-derived data on the right, almost identically featuring the shifted peak and a slightly sharper density decrease than it increased before the peak. The red data reach their maximum $31°$ past the lunar midnight meridian, whereas the green data peak at a longitude of $29°$ behind the lunar midnight meridian.

Overall, the red data projected from the top of the layer delivers the best fit for the LADEE data between the two options, justified by the maximum density value. Peaking at $5.48 \times 10^4 \text{ cm}^{-3}$, the green maximum is too low if compared to the density maximum of 6.64 cm^{-3} of the red data, which is a 2.1% deviation from the LADEE measured density maximum. The minimum density on the dayside based on the better fitting red data equal 2.68 cm^{-3} leading to a 13.6% deviation for the minimum on the dayside when compared to the LADEE data. The ratio between the maximum and minimum densities for the red data equals 24.8, less than the ratio of the LADEE data. Nevertheless, the approximation of the real-life conditions by the simulation is given.

Looking at the plots of the density data projected down from higher layers delivers a plot with the same shape and behaviour as the plot using the data from the first layer and the LADEE data. For example, the peak for the data projected down from the top of the second layer is located at the same latitude as the first layer, and the peak of the third layer is only shifted by $2°$. Only the minima and maxima feature different values. Beginning in layer four, the surface density values at the solar sunrise terminator show a jump, which is increasing for the layers above. The reason for this will be discussed in chapter 5. The corresponding figures can be found in the appendix (Figure A-1, A-2 and A-3).

Figure 4-6 compares the LADEE expected data (red line) with the projected surface density data from each layer normalized by the LADEE expected data. On the left are the densities of each layer displayed on the y-axis and the respective layers on the x-axis. The blue line represents the surface density values projected down from half the height of each layer, the upper limit values represented by the upper limit of the ribbon represent the surface density values projected down from the top of each layer and the lower limit of the ribbon vice versa. It is visible that the upper limit of the surface density is higher than expected for layer 1 and falls closely beneath the expected density. The upper limit's deviation from the expected density stays about 10% for the first ten layers and then increases exponentially. The blue line's deviation stays for about 13 layers in the 20% deviation interval before growing exponentially. This means that the density maximum values projected down from each layer, thereby assuming a barometric scale height with the Chamberlain projection, are valid for the first ten layers if assumed that a 10% deviation is acceptable and for the first 13 layers, and if accepting a 20% deviation and projecting from the middle of each layer height. The deviation of the density values of the elements up to layer ten stays very constant, with all maximum values at about $10 - 20\%$ being too low, which depends on the projection height, which could be a sign of a source rate being assumed too small. However, this allows the data to be analyzed concerning the density distribution in the layers since the deviation can probably be resolved by scaling. The projected surface density data for the minimum surface density occurring in the equatorial band are displayed on the right side. The axes feature the exact quantities as the left plot. As depicted earlier, The minimum projected values show a linear decreasing behaviour at about 13% too high. The linear function intersects the expected value line between the second and third layers. It leaves the 10% deviation interval around layer six and the 20% deviation interval around layer ten. Assuming the barometric scale height with the Chamberlain projection applying to the lunar exosphere, the minimum density data are only valid up to layers six to ten.
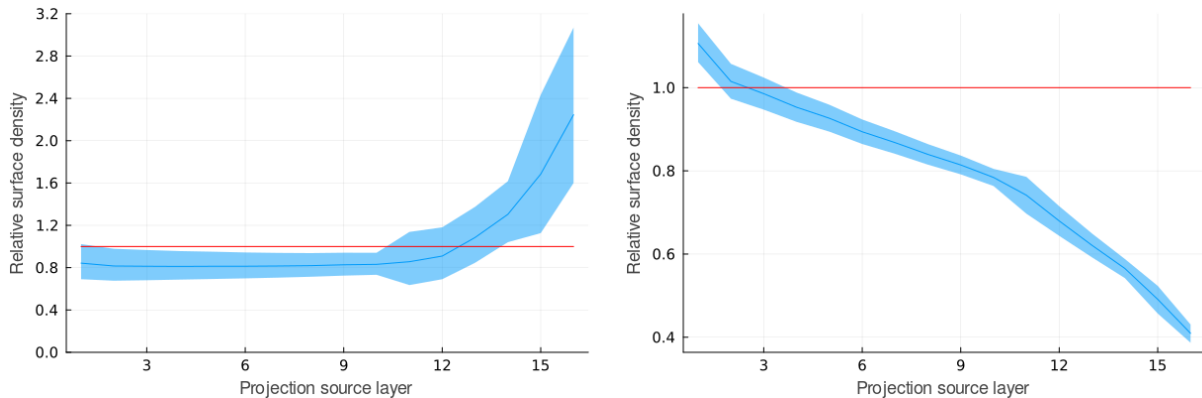
(a) *Projected maximum layer densities compared to LADEE data*

(b) *Projected minimum layer densities compared to LADEE data*

Figure 4-6 : The left figure shows the maximum density data from the equatorial band featured by the LADEE measurements normalized with the maximum density observed by LADEE marked by the red line. On the x-axis, the 16 layers are featured, and on the y-axis, the projected surface density is displayed. The blue graph represents the values for the surface density projected from half of the layer height of each layer. The blue ribbon represents the possible spread, with the upper limit for the density being projected down from the top of each layer and the lower limit from the surface of each layer. It is visible that the deviation of the upper limit equals about 10% and for the blue line, about 20% for the first ten layers. The right figure features a plot with the same properties for the minimum instead of maximum values only. The red line represents the LADEE's expected value again. It is visible that the minimum values of the model are larger than the expected values for the first and second layers and are smaller than the expected minimum density for the layers above. Afterwards, the values constantly decrease in comparison to the LADEE data. Reaching approximately the tenth layer, the deviation of the minimum values from the LADEE data exceeds 20%.

In general, the data presented in and analyzed from Figure 4-5 follow the measured data by LADEE. The development of the data from the equatorial band can be approximated very closely by the model's generated data. The projected data from the first grid layer represents a realistic approximation of the real-life conditions. This is because the first layer of the grid nearly completely covers the measurement altitudes of the LADEE space probe. The maximum densities are scaled down for the first ten layers and, therefore, do not completely feature the values as expected. The location of the maximum and the increase and decrease pattern of the density behave as much as expected. The minima of the density do not fit the expected values. The maximum values,up to layer ten, can be assumed as a reliable approximation. The Chamberlain projection was used to deliver the results for all these approximations because it is the standard method for exospheres like the lunar exosphere. The applicability of the simulated data will be investigated in the following chapter.

The data analysis concerning the validity and statistical value showed that the data of the first ten layers can be seen as a good approximation for the density development as LADEE detected it. Even if the values seem to be scaled down, the ratio between day and night and the development of the density between day and night can be approximated very well, as shown in Figure 4-5. In the following chapter, the meaning of the nearly exponentially rising maximum values and the nearly linearly falling minimum values compared to the expected values by LADEE are further investigated.

5 Results and Discussion

5.1 Data Presentation and Comparison of Different Layers

After analyzing the generated data concerning the statistical properties and verifying the validity to draw reliable conclusions, the density values of the grid elements will be analyzed. As described in chapter 3, the grid consists of $129\,600$ elements with 16 layers, 180 elements in the longitudinal direction and 45 elements in the latitudinal direction. Each element contains the density data acquired from the post-processing in chapter 4. The density data, multiplied for the comparison with the LADEE data with the adjustment factor of 2.5 for average values, will be analyzed in this chapter without this adjustment, to analyze the real data generated by the model. The analysis also neglects the influence of the endogenic sources, which were excluded from the model assumptions.
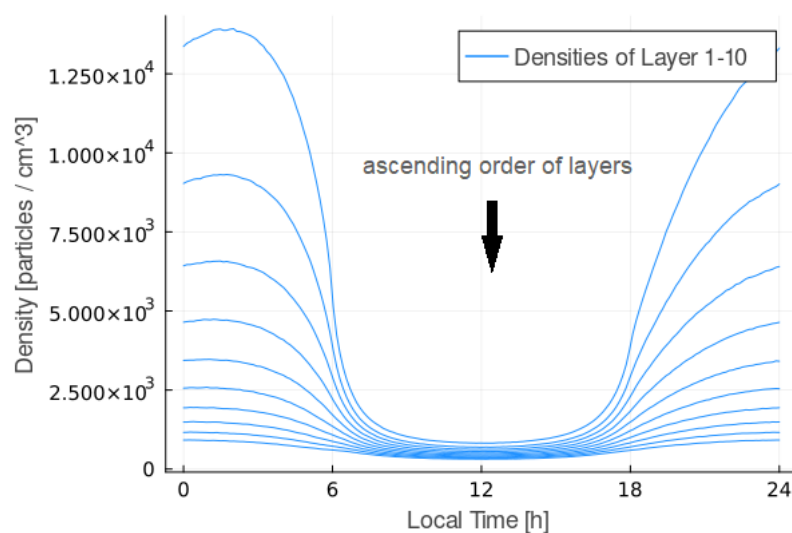

Figure 5-1 : The figure shows the equatorial densities of the first ten layers on the y-axis. The x-axis carries the local time. It is visible that the density on the nightside is much higher than on the dayside. For the top line, which corresponds to the first layer in the numerical grid, the values are about ten times larger, for example. The density difference between each layer decreases, moving downwards in the figure. The arrows in the figure show that the downward movement in the figure corresponds to an increase in altitude in the numerical grid. Furthermore, the difference in the density values between the layers is much higher on the nightside than on the dayside, where the lines are very close together. The tendency of the lines to decrease their distance increases around the solar terminators. Therefore, the density numbers become more similar (sunrise) before the differences increase again (sunset). The first four layers show a distinguished maximum at about 2 hr local time, which flattens out beginning in the fifth layer.

Figure 5-1 shows the equatorial density data of the first ten layers in one diagram. On the y-axis, the density is displayed, and on the x-axis, the local time on the lunar surface. The ten graphs represent the density data of the first ten layers of the numerical grid. The uppermost line belongs to the lowest layer in the grid. It is visible that the density on the nightside is much higher than on the dayside. For the lowest layer, the ratio is about ten. Then, it decreases with every layer above. The first four layers show a more or less distinguished maximum at about 2 hr local time, which equals 1.648×10^4 cm^{-3} for the maximum of the top line corresponding to the lowest layer. The maximum density in the second layer equals 1.021×10^4 cm^{-3} only, which is about 60% of the density of the layer below. The maximum no longer exists from the fifth layer upwards, even if looking closer at the data. The higher a layer is located, the less the density decreases towards the next layer above, compared to the layers below. This effect is far more expressed on the nightside than on the dayside.

The density numbers are moving much closer around the lunar sunrise terminator. In contrast, the opposite effect can be observed around the lunar sunset terminator as depicted in Figure 5-2. This figure shows the dayside part of Figure 5-1 in the interval between $6\,hr$ and $18\,hr$.
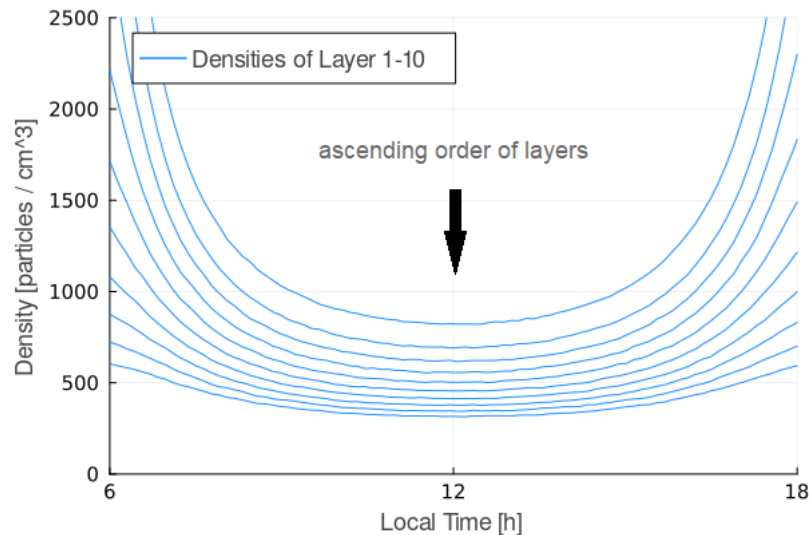

Figure 5-2 : The figure shows a cut-out of Figure 5-1 for the local times between $6\,hr$ and $18\,hr$, which are displayed on the x-axis. The y-axis shows the density values again. It is visible that the densities of the bottom layers in the figure (equivalent to the layers of high altitude in the exosphere) are closer together than the densities of the top layers in the figure (equivalent to the low layers in the exosphere).

The difference in the density values of the dayside and nightside originates in the start velocity of the helium particles. Due to the large temperature differences between day and night, the velocity sampled from the Maxwell-Boltzmann-Flux distribution is much higher on the dayside, which, on average, allows the particles to reach layers of high altitude. On the nightside, the particles accumulate in the lower exospheric layers, which leads to the high density gradient inside the layers between the nightside and the dayside, which is clearly visible in the figures above.

Figure 5-3 visualizes the density distribution in the first layer of the grid with the local time displayed on the x-axis and the latitude on the y-axis. It is visible that the density is much lower on the dayside than on the nightside in the equatorial regions, as already observed in Figure 5-1. This tendency is visible in this figure for all latitudes. On the dayside up to the latitude of $70°$, values below 2500 particles per cubic centimetre (dark blue areas)are visible, whereas the density on the nightside shows values of about $15\,000$ particles per cubic centimetre (bright yellow areas). The transition around the solar terminators is wider at $18\,hr$ local time than at the solar sunrise terminator, which means that the density at the sunset terminator rises slower than the density falls around sunrise. This observation is visible in Figure 5-1, too. It can be explained by the hotter temperature at sunset because the lunar surface is still warm due to its thermal inertia. If the transition zone was divided exactly at the sunrise terminator, it would be found that the part of the dayside would be about as wide as the other half of the transition zone on the nightside. At the lunar sunset terminator, the dayside half would be thinner than the nightside half due to the thermal inertia. The terminators can be precisely determined from the colour change there, which implies a very high-density gradient. This can be seen in Figure 5-1 as well.

In the polar regions (above $85°$), the density on the dayside is slightly higher than on the rest of the dayside. This development begins at about $70°$ with a bow-like shape visible in the figure. This can be explained by taking the dimensions of each dayside grid element into account. Since the layer forms a sphere around the Moon, the polar elements are located just by or near the corresponding nightside elements. This means the density transition zone can be expanded on the polar elements since the particles can easily reach the dayside polar elements, even at $12\ hr$ local time with their short hops from the nightside.
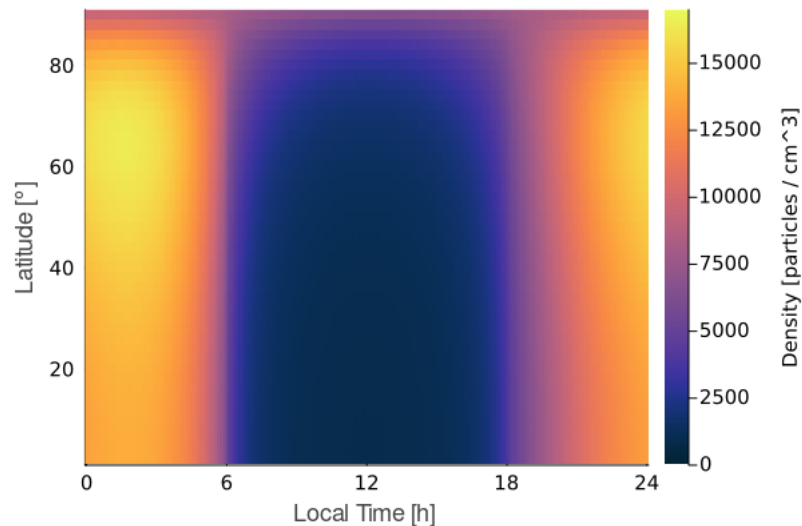

Figure 5-3 : *The figure visualizes the densities of the elements of the first grid layer ranging up to an altitude of* 50 km. *It is clearly visible that the density on the dayside is much lower (dark blue colours) than on the nightside (bright yellow colours). Around the solar terminators, a transition zone is visible, which is wider around the sunset than around sunrise. This can be explained by the thermal inertia of the lunar surface, which allows the particles to perform higher hops shortly after sunset than just before sunrise. Since the elements of the grid become smaller with increasing latitude, and the polar elements border or belong to the nightside just like the near-terminator elements, the density is increased there compared to the other dayside elements far away from the terminators. The reason for this is that the particles from the nightside, which are performing short and not very high hops, are able to reach these elements more easily.*

This distribution of the density in the first layer, with high density values on the nightside and low density values on the dayside, shall be seen in the heatmaps for the following layers as well, as it is depicted in Figure 5-1, with lower densities only. Figure 5-4 shows the respective heatmaps of layer two on the left and layer four on the right, which corresponds to the altitudes of 50 km to 100 km and 150 km to 200 km. On the x-axis, the local time is displayed, and on the y-axis, the latitude is displayed. The colour scale is the same as the scale of Figure 5-3 for better comparability. The density shows the same development throughout the respective longitudes and latitudes as the density in layer one. The density transition zone is clearly visible in both plots, which separates the dayside at the terminators and the poles from the nightside. The density in the left plot of layer two is on the nightside about twice as high as in layer four in the plot on the right. The significant difference to Figure 5-3 is that the transition zone at the sunset terminator is thinner and no longer much wider than the transition zone at the sunrise terminator. This effect is more distinct for the right figure corresponding to a higher layer. The reason for this is that the particles sampled in higher layers do not necessarily originate from the surface below. This shall be assumed because of the following: if the surface is still warm, the particles, on average, gain more kinetic energy, meaning that they perform larger hops. This means that in layer one, where the particles necessarily need to be sampled, the density decreases.

The probability that a particle performs a vertical hop and is sampled in the elements of the exospheric column above is not very high, so it will probably be sampled in elements nearby (in the next higher layer). This means the effect observed for layer one, where it led to a distinctively more expansive transition zone around sunset, is blurred for the layers above.


(a) *Density heatmap of layer 2 (*50 - $100 \mathrm{\,km}$*)*   (b) *Density heatmap of layer 4 (*150 - $200 \mathrm{\,km}$*)*
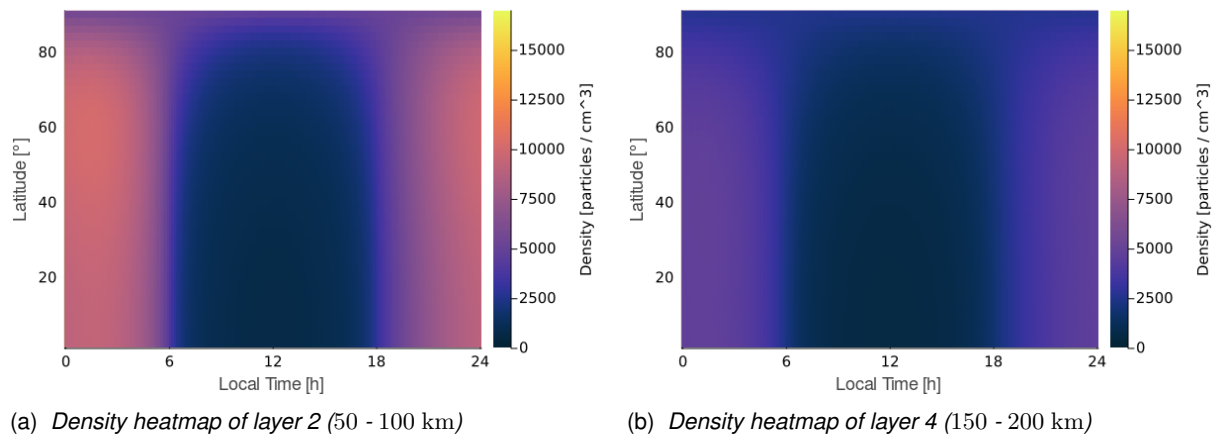
Figure 5-4 : The two figures display the density values for layer 2 (50 - $100 \mathrm{\,km}$*) on the left and layer 4 (*150 - $200 \mathrm{\,km}$*) on the right. The colour scale is the same as the scale of Figure 5-3 for better comparability. The two layers show the same characteristics as layer one, with a decreased amount of density values. The major difference is that the transition zone, which was wider at the lunar sunset terminator than at the lunar sunrise terminator in layer one, becomes thinner for layer two and even thinner for layer four and then has approximately the same width as the transition zone at the lunar sunrise terminator.*

The development of the densities above the tenth layer is depicted in Figure 5-5. The line at the top represents layer 11, and with each line below the layer number increases. The left figure shows the equatorial densities of the layers 11 - 16 with the density on the y-axis and the local time on the x-axis. The right figure shows the heatmap of layer 13, which is highlighted in Figure 5-5b as the continuous blue line. Displayed on the x-axis of the right plot is the local time, displayed on the y-axis is the latitude, and the colour scale represents the density values between 150 and 320 particles per cubic centimetre. In the left plot, it is visible that the density difference between the dayside and nightside is decreasing when comparing layer 11 and layer 12. In layer 12 (the dashed blue line above the continuous blue line), a local maximum is forming at the lunar sunrise terminator, which becomes a global maximum in layer 14. In layers 15 and 16, the density on the dayside becomes higher than on the nightside. This can be explained by the high amount of kinetic energy, which is necessary to reach these heights and is, on average, achieved in higher numbers on the dayside due to the high surface temperatures.

Based on these findings, it is highly probable that most of the particles sampled in these altitudes originate from dayside starting locations and are performing very high hops, which let them be sampled in the nightside elements. The heatmap of layer 13 on the right side confirms the formation of local maxima observed in the left figure, which can be seen at $6 \, hr$ local time at the lunar sunrise terminator, with the red area surrounded by a more blue area. In general, the density is not as orderly distributed in layer 13 as it was observed in layer 1 (Figure 5-3), for example.
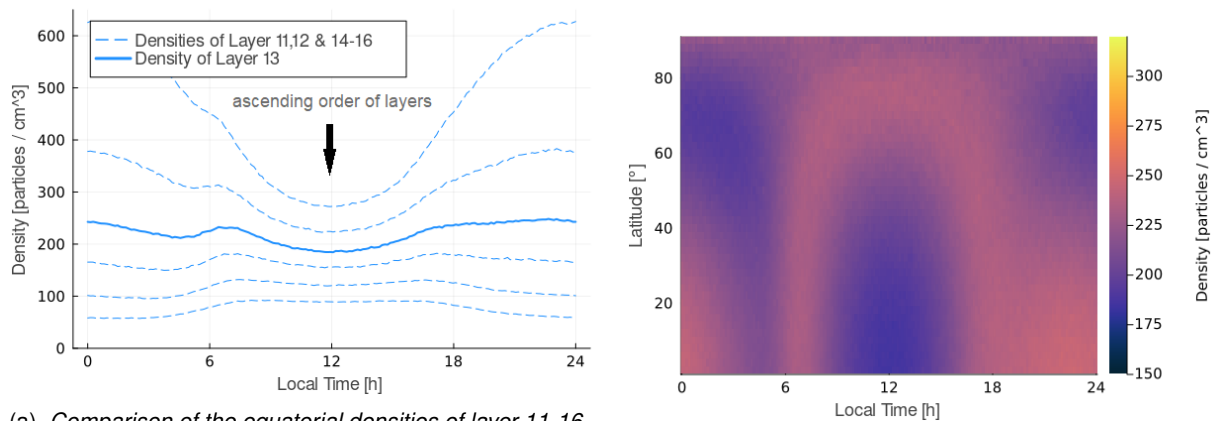
(a) *Comparison of the equatorial densities of layer 11-16 (above* 1000 km*)*

(b) *Density heatmap of layer 13 (*1250 - 1375 km*)*

Figure 5-5 : Displayed on the left are the equatorial densities of the layers 11 - 16, which cover the altitude between 500 km and 1500 km. Depicted on the right is the density heatmap of layer 13. The local time is displayed on the x-axis in both figures, whereas the y-axis in the left figure carries the density values and, in the right one, the latitude. The colour bar represents the density values in the right figure. It is visible that the pattern of the equatorial density of layer 11 resembles the patterns expressed by the layers below, being flatter, however. The other layers, on the other hand, are more balanced in terms of the ratio of the density of the nightside and dayside. Beginning in layer 12, a local maximum forms around the solar sunrise terminator, which becomes a global maximum in layer 14. The continuous blue line represents layer 13, which is in total depicted in the heatmap on the right. It is clearly visible there that the local maximum is forming at a local time of 6 hr, represented by the red colour, laterally surrounded by blue colours. Additionally, the density is no longer as orderly distributed as seen in the lower exospheric layers, as to be seen in Figure 5-3, for example.

To summarize, Figure 5-5 shows that the density begins to balance beginning in layer 11 ranging from 500 km to 625 km. In the layers 13 and 14, between 750 km to 1000 km, the density between day- and nightside is balanced with slight fluctuations. In the remaining grid layers 15 and 16, between 1000 km to 1500 km, the density on the dayside is higher than on the nightside.

5.2 Comparison within the Layers

The development of the density values within the layers is depicted in Figure reffig:Density Inside Layer. The densities in each layer are shown for different latitudes, in detail for $0°$ (equatorial), $30°$, $60°$ and for the polar elements for $90°$, in each figure for a different layer. Figure 5-6a shows a map of the lunar temperature, taken from *Smolka, 2023*, and based on the analytical function for the lunar surface temperature by *Hurley, 2015* [8], [9]. The figure was modified by marking the respective latitudes with red lines, from which the density data were taken, for plotting the other three figures.

Figure 5-6b, 5-6c and 5-6d show the development of the density whithin layer 2, 7 and 16. Displayed on the x-axis is the local time, and on the y-axis are the density values. The blue line represents the density for the latitude of $0°$, the orange line for $30°$, the green line for $60°$ and the pink line for the polar band at $90°$. In Figure 5-6b (layer 2, between 50 to 100 km), it is visible that all densities, with the exception of the polar density, are very close together. The green line marks slightly larger values, followed by the orange line, which means that the density slightly increases when starting at the equator and moving latitudinally upwards to the poles. This can be explained by the decreasing temperature, which decreases the start velocity of the particles on average.
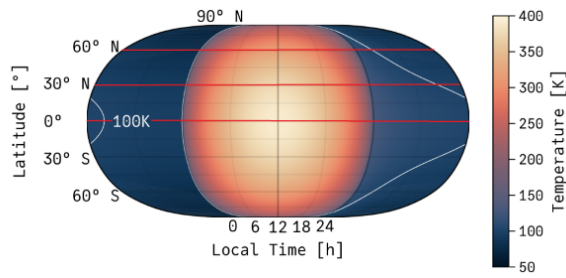
(a) *Lunar surface temperature map with marked latitudes, taken from Smolka, 2023 and modified [9]*
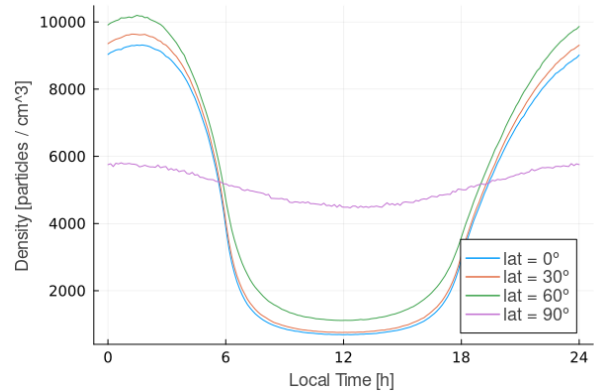
(b) *Densities of different latitudinal bands - Layer 2*
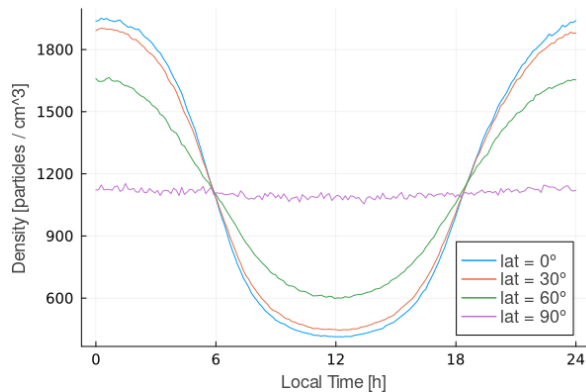
(c) *Densities of different latitudinal bands - Layer 7*
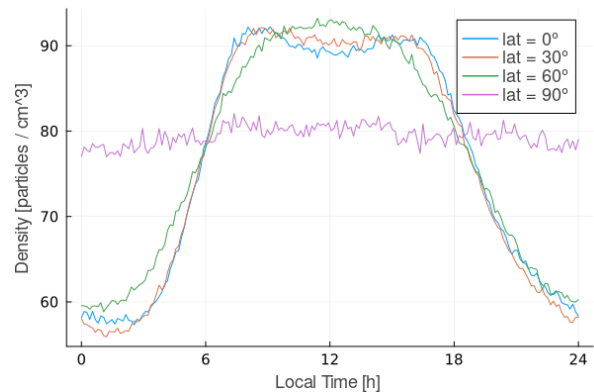
(d) *Densities of different latitudinal bands - Layer 16*

*Figure 5-6 : The figure at the top left shows the temperature map taken from Smolka, 2023 that is based on the analytical surface temperature function by Hurley, 2015, which was introduced in section **??**. From each layer, displayed in the other three figures, four samples of latitudinal bands ($0°$, $30°$, $60°$, $90°$) were taken. The density is displayed on the y-axis in all plots and individually scaled to represent the respective maximum densities occurring in the layer. The local time is displayed on the x-axis. It is visible in Figure 5-6b that the densities develop with closely related density values for the lower three bands. The polar band develops nearly constantly with a flat hollow on the dayside. For layer 7, displayed in Figure 5-6c, only the two bands of lower latitude show closely related density values, whereas the $60°$ band's values are lower on the nightside and higher on the dayside. The polar band shows nearly constant density values. In layer 16, the conditions are reversed, as already seen in Figure 5-5a, and the density on the dayside is higher than on the nightside; the latitudinal bands show similar values again. It is visible that due to the low density values and the mid-height of about $1375\,\mathrm{km}$ of layer 16, the quality of the data is not as reliable as the data of the lower layers, which is indicated by the small variations the lines are showing. However, the tendency of the density data to be higher on the dayside is clearly expressed as expected.*

A lower start velocity means that the particles perform smaller hops and are, in total, being sampled in higher quantities in the low layers, which is the reason for the higher density values observed here. The polar density values show an almost constant behaviour with a flat hollow on the dayside. The reason for this is the surface temperature again. On the polar dayside, elements are hotter than the polar nightside elements, which means that the particles perform higher hops and are not sampled in the low layers as much as the particles on the nightside. However, because of the proximity to the nightside elements, many particles originating from the nightside are sampled in the dayside elements, which increases the density there.

Figure 5-6c shows the density of the four latitudes in layer 7, which covers the altitude of 300 to 350 km. The plot properties are the same as in the plot for layer 2; only the scale of the y-axis was adapted to the density values of layer 7.

The polar line shows almost the same behaviour with a nearly constant development. This can be explained in the same way as for the previous figure, with the slow initial particle velocities being slightly higher on the dayside, which would lead to a decreased density on the dayside compared to the nightside but is balanced through the proximity to the nightside. The density in the $0°$ and $30°$ bands shows similar behaviour to the previous figure, as well as being scaled down only. The $60°$ band, on the other hand, shows a lower density on the nightside and a higher density on the dayside when compared to the two other bands. This can be explained using the surface temperature again. Looking at Figure 5-6a, the surface temperature on the nightside lays below the 100 K limit for most of the time for the latitude of $60°$, whereas the two other latitudinal bands feature values over the 100 K limit for a local time between 18 and $24 \ hr$ and lay below this limit between 0 and $6 \ hr$, but still higher than the values for the $60°$ band. In layer two, the effect of the lower start velocity was not as expressed as it is now for layer 7. Due to the higher altitude, more particles are sampled in the $60°$ band on the dayside in layer 7 since they are starting to become much slower than the particles from the other bands in the high layers and, thus, are sampled more often in the respective elements since they spend more time there while crossing it. With the growing height, this effect increases. On the nightside, on the other hand, the temperatures are so low that fewer particles reach the altitude of layer 7 in the $60°$ band than in the other two bands. This leads to a reduced density there.

The density development of layer 16, the top layer, is shown in Figure 5-6d. The properties of the plot are the same as the previous two above, with the y-axis being scaled further down only. Since the density is very low in the altitude of 1250 to 1500 km with less than 100 particles per cubic centimetre, the accuracy of the data is limited, which is visible in the plot as the lines are not as smooth as seen in the previous plots. Additionally, this layer has a layer height of 250 km, which is five times as large as each of the first ten layers. This means many particles are summed up in this layer, further limiting the meaningfulness of the exact density values. The plots show clearly, on the other hand, that the density on the dayside exceeds the density on the nightside, as primarily depicted in Figure 5-5a. The density values develop in a very similar pattern for all latitudinal bands except the polar band. The about 50% higher density on the dayside is the result of the temperature just being high enough on the dayside to reach altitudes that high. Since a particle, which is sampled in an element in layer 16, originates only in the minority of cases from the surface directly below, the generally constantly developing density on the dayside arises from the mixture of particles, which originate from different locations of the dayside. Since there is the possibility that a particle gains much lateral velocity, there can be particles found in layer 16 above the nightside since the ballistic trajectory on a sphere allows it to gain height in the radial direction, even if the local starting velocity is rectangular to the radius. The polar density develops almost constantly as expected, only that it is now reversed to the polar density of layer 2. This is the result of the proximity to the dayside elements, which have a much higher density than the nightside elements.

A major similarity of all density plots is that the density plots of the smaller three latitudes intersect the polar latitude at the solar terminators.
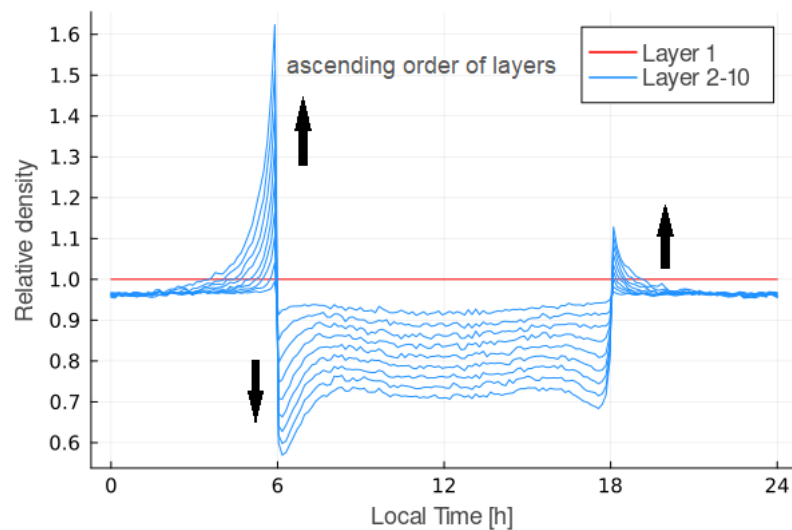
Figure 5-7: Depicted in this figure are the equatorial densities projected down to the surface and normalized with the projected density of layer one. For the projection altitude, which is the reference height for each projection, the mid of each layer was used. On the x-axis, the local time is displayed, and on the y-axis, the relative density to layer one. The other nine lines can be assigned to each layer, with the most extreme in numbers (the maximum line around the sunrise and sunset and the minimum line on the dayside) being the highest exospheric layer. On the nightside, between $20\,hr$ and $3\,hr$, layer 2 to 9 show a deviation of about 4%. On the dayside, layer 2 shows a deviation from the projected density of layer one of about 8%, which increases for each layer above for about 2 to 3%. Layer 10 shows, therefore, a deviation of about 30%. Around the solar terminators, there are two visible peaks. The sunrise peak consists of an exponential rise followed by an overshooting downwards at the terminator with logarithmic growth to the dayside values. A noticeable detail is that the nearly exponential functions show the same equidistance as the dayside relative densities of layers 2 to 10. Behind the sunset terminator, the relative density decreases in the same pattern as it rises at the sunrise peak, thereby being mirrored at the subsolar meridian, with only a smaller overshoot.

This is the result of the high temperature gradients that lead to the existence of the transition zone that can be observed in Figure 5-3 and 5-4. When looking closely at the intersections, it is visible that the intersection with the polar density lies exactly at the solar sunrise terminator but closely behind the solar sunset terminator. This reminds of the slightly wider transition zone, which is the result of the thermal inertia that the lunar surface expresses here. The polar dayside elements lay directly next to the polar nightside elements at the north pole (the grid only covers the northern hemisphere), where the lunar sunset and sunrise terminator meet. This is the reason for the same density at the poles as to be found at the terminators. Since the width of the transition zone of the solar sunrise terminator measures about $180\,\mathrm{kilom}$ and the width of the area covered by the polar elements, in latitudinal direction, measures about $120\,\mathrm{km}$ maximum, the polar elements lie inside of the transition zone.

5.3   Barometric Density Development

In subsection 2.4.2, it was introduced that the projection of density data is made using the formula developed by *Chamberlain, 1963*, which is a modified version of the barometric formula.[14] The modified version is adapted to the ballistic movement of the particles.
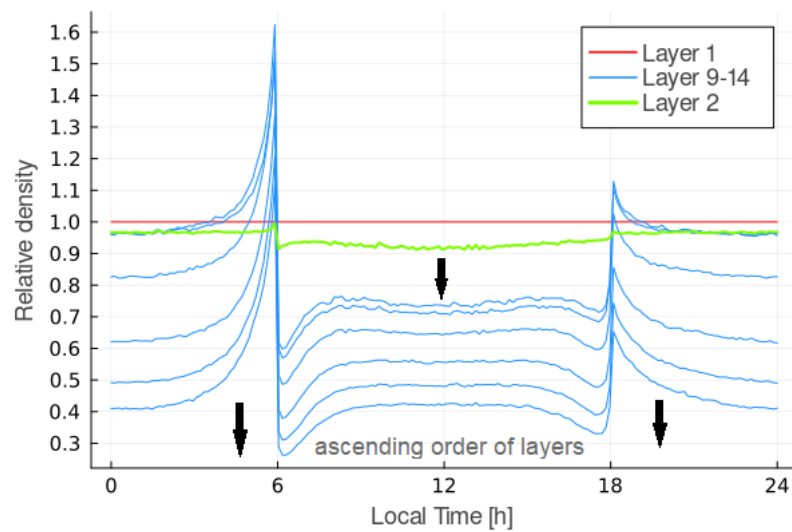
Figure 5-8 : The setting of the figure is the same as for Figure 5-7, with the projected surface density relative to the projected density of layer one on the y-axis and the local time on the x-axis. The constant red line represents the surface density projected from layer one, which equals one, after being normalized with itself. Displayed in bright green is layer two to show the small deviation from layer one and the small peaks of this layer. Displayed in blue are the layers 9 to 14. Above layer 10, the layer height increases from 50 km to 125 km. It is visible that the space between the lines on the dayside increases as well for the layers below layer 10 in the figure. The four lower blue lines corresponding to the layers 11 - 14 show a deviation of about 7% instead of about 2 to 3% between the layers 9 and 10. The deviation of the relative density of the layers 11 to 14 on the nightside does not show the same behaviour as the deviation of the lower ten layers. Instead, the deviation is increasing with a growing layer altitude.

Figure 5-7 shows the equatorial surface densities of the layers 2 - 10, projected down, taking the middle of each layer as the reference height. The data are normalized with the projected surface density of layer 1. Therefore, on the y-axis, the projected surface density relative to the projected surface density of layer one is displayed. The local time is displayed on the x-axis. The red constant line is the projected surface density of layer one, which equals one after the normalization with itself. The other 9 lines are each assigned to the 9 remaining layers, with the most extreme line (the line with maximum values on the nightside, especially around the terminators and the minimum line on the dayside) assigned to the uppermost exospheric layer, which is layer 10. The layers are then assigned in decreasing order to the next inner line. On the nightside, between 20 hr and 3 hr, the relative density of the layers 2 to 9 all show a deviation of about 4% to the reference density. On the dayside, the deviation from the reference density equals about 8% and for every layer above in equidistant steps about 2 to 3% more, leading to a deviation for layer 10 of about 30%. Around the solar terminators, two peaks are visible. The sunrise peak is characterized by an exponential rise between 3 hr and 6 hr with an overshooting jump below the dayside values, which are reached with approximately logarithmic growth. The peak pattern at the solar sunset terminator can be described as mirrored at the subsolar meridian, with smaller peaks only.

Figure 5-8 shows the projected surface densities of the layers 2 and 9 to 14 relative to the projected surface density of layer one, which is, relative to itself, represented by the red line equaling one. Displayed on the x-axis is the local time, and on the y-axis is the relative density. The projected surface density of layer two is represented by the bright green line. It is visible that the peaks are tiny compared to higher exospheric layers. The deviation stays within 10% for all local times.
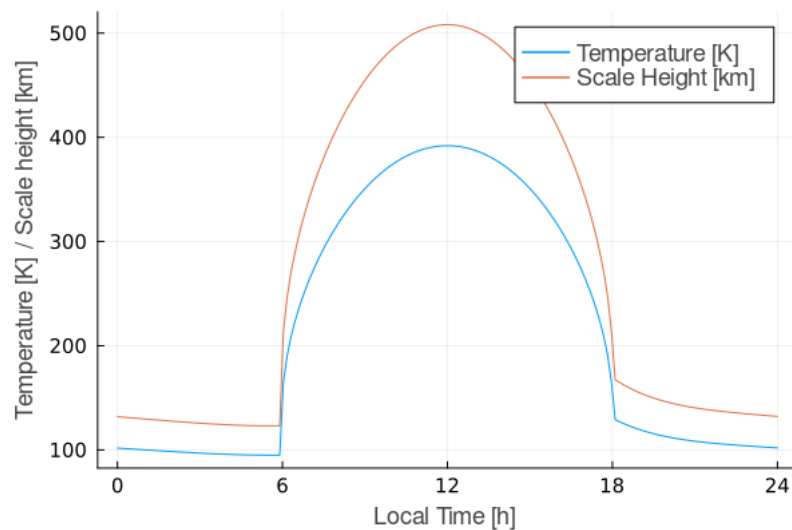
Figure 5-9 : Visible in the figure are two graphs, where the blue one shows the equatorial surface temperature of the Moon and the orange one the corresponding scale height, assuming an isothermal exosphere. On the x-axis, the local time is displayed, and on the y-axis, the scale height and the temperature share the same scale. Around the solar terminators at $6\ hr$ and $18\ hr$, the temperature and scale height show very high gradients with a sharp bend right at the terminators.

The blue lines represent the layers 9 to 14. On the dayside, the space between the lines increases beginning after layer 10. In the grid, the layer height increases after layer 10 from $50\ \mathrm{km}$ to $125\ \mathrm{km}$. The deviation increases for each layer below layer 10 in the figure to about 7%. On the nightside, the relative density of the layers 11 to 14 does not show the same behaviour as the layers below in the exosphere. Instead, with every layer up in the grid, the deviation increases. The effects responsible for the depicted phenomena and patterns are discussed in the following subsections.

5.3.1   Exponential Deviation between Relative Layer Densities at the Solar Terminators

A striking detail in Figure 5-7 are the peaks around the terminators. Between 3 and $6\ hr$ local time and 18 and $20\ hr$ local time, the deviation from the reference density shows a strange development. This pattern is independent of the choice of the reference density, as depicted in the previous subsection. Figure 5-9 shows the development of the equatorial surface temperature in kelvin (blue graph) and the scale height in kilometres belonging to it (orange graph). Displayed on the x-axis is the local time, and on the y-axis is the temperature for the blue graph and the scale height for the orange graph. It is visible that the temperature falls rapidly near the solar terminators on the dayside, as does the scale height. This means that the scale heights of neighbouring exospheric columns can differ a lot, which means that the density is projected very differently down to the surface. If two elements feature very similar densities, however, the surface temperature, on the other hand, is very different below them, the exospheric column of the colder element features a much smaller scaler height (in the isothermal exosphere, the temperature of an element equals the surface temperature below, introduced in subsection 2.4.2). This means the same density will be projected to a much higher surface density than the density of the hotter element. This is the explanation for the very large jump down with the overshooting below the surface density values.

The peak at the solar terminators grows with growing exospheric altitudes. There are two mechanisms responsible for this behaviour. In the exospheric elements just before the sunrise terminator, the surface temperature is very low, which leads to a very low scale height. When projecting the density of the first layer up to the higher exospheric layers using the Chamberlain formula, the expected outcome would be a very fast decreasing density due to the low scale height. Since the surface of the elements just behind the terminator is much hotter due to the solar radiation, many particles with high velocities originating from the Sun-lighted surface elements will cross the terminator and reach the upper layers of the colder area just before the terminator. This means there are particles present in the upper exospheric layers just before the terminator, which shall not be assumed to exist, at least if the Chamberlain formula is assumed since the formula does not take the high temperature gradients into account. This effect is then intensified by the small scale height, which increases the projected surface densities even more. At the solar sunset terminator, this effect is visible as well, but less as strong as at the sunrise terminator. This is because the temperature jump is not as large as at the sunrise terminator due to the thermal inertia of the surface.

The overshooting behaviour below the dayside density can be explained with regard to the same effect that is responsible for the peaks. The elements near the nightside show a lower density since the particle flow from the neighbouring nightside elements for these particular dayside elements is much lower than it would be from neighbouring dayside elements. The higher a layer is located in the grid, the more it becomes relevant since the particles originating from the nightside, on average, do not perform as high hops as the particles originating from the dayside. As it was described in Figure 5-8, the peaking and the overshooting are very small for the second layer (bright green line) since this layer is not very much influenced by the effect of the fast dayside particles due to its low exospheric altitude.

5.3.2 The Linear Growing Dayside Deviation and the Extra Deviation of Layer 1

In the two Figures, Figure 5-7 and Figure 5-8, it is visible that the deviation of the relative density on the nightside is linearly growing with a specific gradient for layers 1 to 10 and a higher gradient for the layers 11 to 14. Therefore, the density is lower in the elements than expected when projecting the density of layer one up to the layers above. This behaviour can be explained by the mixing of particles with different temperatures in the same element. The Chamberlain formula assumes an isothermal exosphere, which means that the particles have the same temperature as the surface right below them. Therefore, the scale height for the particles is dependent on the surface temperature only. This model can be applied to particles near the surface, which move on trajectories that are not very high, and the particles do not perform jumps into areas where the temperature is entirely different. This is why the relative densities of layers 2 to 10 are almost equal on the nightside. The Chamberlain formula applies here. In fact, the particles do not adopt the surface temperature of the element below them. They carry the surface temperature of the initial location, which they gained through thermal accommodation as introduced in subsection 2.3.2. This means, in reality, the scale height decreases with increasing altitude as a result of mixing processes of particles with a lower temperature, so the density decreases faster, as it should be when applying the Chamberlain formula.

Layer one shows a constant deviation on the nightside and an extra deviation on the dayside. The extra deviation of layer one is higher on the dayside than on the nightside. This can be evidence of a dependency on the initial velocity of the particles since this is the significant difference between day and night. This effect can probably be explained with the numerical properties of the simulation, the layer height of the first layer ($50 \ \mathrm{km}$) in connection with the sample step of $15 \ \mathrm{s}$ and the average start velocities of about $1 \ \mathrm{km \, s^{-1}}$. The particles can very often be sampled in the first layer, which leads to an elevated density.

5.4 Analysis of the LADEE Comparison

In chapter 4, the model data were compared to the data collected by LADEE. In Figure 4-6, the maximum and minimum values of each layer from the $\mp 23°$ equatorial band were compared relative to the expected values based on LADEE. In Figure 4-6, it was found that the minimum data show a linear degressive behaviour with an increasing negative gradient above layer 10. This behaviour can be explained now using the findings from Figure 5-7 and Figure 5-8. The projected surface density was found in these Figures to deviate from the reference density with linear growth, moving up in the layers, with a higher gradient after layer 10. Since Figure 5-1 and Figure 5-5a show that the density minimum is located on the dayside for layer 1 to 13, the linear growing deviation found in Figure 5-7 can be applied here. For layers 14 to 16, the density minimum is not located on the dayside, but since the density is very similar comparing the day and nightside and does not differentiate as much as for the lower layers, the dayside values can be taken into account here, which gives the opportunity to apply the linear degressive behaviour again.

The maximum values of each layer, as visible in Figure 5-1 and Figure 5-5a, are located on the nightside at about $2 \ hr$. This means, when looking at Figure 5-7 that the deviation from the reference value equals a constant value, which leads to the findings of Figure 4-6 for the first ten layers. The maximum values then shift to the solar sunrise terminator as depicted in Figure 5-5a, which explains the exponential growth of the maximum relative surface density in Figure 4-6 as observed in the same way in Figure 5-7. These results explain the behaviour of the data compared to the LADEE data and support the validity of the data in all layers. The LADEE data were very well reproduced by the projected surface densities of layer one, which covers almost the same heights that LADEE covered, too, with a density value deviation of 2.1% to 13.6% only. The deviations of the projection of the layers above from the LADEE data can now be explained as the result of the deviation of the real-life conditions from the Chamberlain formula idealization.

6 Conclusion

This work aimed to develop a three-dimensional model of the helium density in the lunar atmosphere. To achieve this, a Monte Carlo approach was used to simulate the ballistic hops of the helium particles. Before analyzing the generated data regarding the helium particle density, a statistical evaluation was applied, asserting the convergence of the Monte Carlo simulation and the statistical verification of the density data.

Additionally, the data were compared to helium surface density data, which were calculated based on the experimentally collected density data of the LADEE space probe. The results showed that the data from the layer of the numerical grid, which covers the same heights in which LADEE examined the lunar exosphere, showed an exact representation of real-life conditions. The projected densities of the layers above showed constant deviations for the maximum and minimum values, a linear growing deviation to smaller density values than expected by the Chamberlain formula. These were found to be the result of mixing processes of particles with different temperatures, which leads to a modified scale height that deviates from the constant scale height in the isothermal atmosphere, which is based on the surface temperature.

Overall, it was found that the density on the nightside is higher than on the dayside for altitudes up to 750 km. This condition was explained by the low start velocities of the particles, which led to the accumulation on the nightside due to the short and low hops of the particles. Above that, the density is balanced on the global scale, and it shows local maxima around the solar sunrise terminators. Above 1000 km, the density on the dayside is higher than on the nightside since only particles with high starting velocities gained on the hot dayside reach these heights.
Furthermore, the density dependency on the latitude grows with an increasing layer altitude since the temperature decreases if moving from the equator to the poles. Hence, the particle start velocity decreases, and the particles' hops are not as high as at latitudes near the equator. Therefore, the density on the nightside in high latitudes is lower than in low latitudes. On the dayside, the density in higher latitudes is increasingly higher than in low latitudes for a growing layer altitude since the slower particles are accumulating in lower layers compared to fast particles. In very high layer altitudes (around $1500 \ \mathrm{km}$), the density is balanced again.

7 Outlook

The simulation developed for this work offers the means to determine the helium particle density at a given location in the lunar exosphere below the limit of an altitude of 1500 km. However, this model can be easily applied to generate data for other monoatomic species, such as the noble gases neon and argon. Furthermore, a modified model would be able to simulate other molecular species as well.

If the physical complexity of the simulation was increased, various effects could be taken into account, which have not been assumed in this work. For example, the rotation of the moon or the local electric and magnetic fields on the surface could be included in the calculations, and the influence of the Earth's magnetic field could also be simulated if ions were investigated. One could also investigate the extent of the influence of interstellar sources such as the Local Interstellar Cloud or the helium focussing cone of the Sun. The Local Interstellar Cloud, a cloud of interstellar particles, surrounds our solar system and has a diameter of several parsecs. Its properties were studied by analysing of the UV spectrum absorption in the light of stars in the cosmic neighborhood.[17] The Sun moves with a relative speed of 26 km s^{-1} through the Local Interstellar Cloud, which Gloeckler and Geiss found to have a neutral helium density of 0.0154 cm^{-3}.[18], [19] Since, for helium, the Sun's gravitational pull is much stronger than the solar radiation pressure, the interstellar gas atoms can enter the solar system undisturbedly. Moving through the Local Interstellar Cloud, the Sun collects helium atoms in its wake and forms a concentrated cloud called a focusing cone. The cloud is shaped like a cone positioned with the base at the Sun and the top away from the incoming particle stream and reaches out past 1 AU with increasing helium density and thus past the orbit of the Earth and Moon.[19]

The numerical parameters of the simulation could also be further investigated. For more accurate data, the layer heights of the grid could be reduced to obtain more accurate results. However, this also requires a reduction in the time sample step because, if assumed otherwise, it could result in particles that skip specific layers due to their high speed without being sampled there. The density behaviour in the high grid layers can also be further investigated. However, the measures mentioned inevitably lead to a much higher required computing power, which would require additional simplifications to be reduced.

References

[1] C. Grava, D. M. Hurley, P. D. Feldman, *et al.*, "LRO/LAMP observations of the lunar helium exosphere: Constraints on thermal accommodation and outgassing rate," *Monthly Notices of the Royal Astronomical Society*, vol. 501, no. 3, pp. 4438–4451, 2021.

[2] M. Benna, P. R. Mahaffy, J. S. Halekas, R. C. Elphic, and G. T. Delory, "Variability of helium, neon, and argon in the lunar exosphere as observed by the LADEE NMS instrument," *Geophysical Research Letters*, vol. 42, no. 10, pp. 3723–3729, 2015.

[3] H. Karttunen, P. Kröger, H. Oja, M. Poutanen, and K. J. Donner, *Fundamental Astronomy*. Berlin, Heidelberg: Springer Berlin Heidelberg, 2017.

[4] S. R. Taylor, C. M. Pieters, and G. J. MacPherson, "7. earth-moon system, planetary science, and lessons learned," in *New Views of the Moon*, B. L. Jolliff, M. A. Wieczorek, C. K. Shearer, and C. R. Neal, Eds., De Gruyter, 2006, pp. 657–704.

[5] A. Smolka, "Lunar exosphere simulation: Modeling and simulation of our moon's surface-bounded exosphere," 2022.

[6] J. L. Kohl and S. R. Cranmer, *Coronal Holes and Solar Wind Acceleration*. Dordrecht: Springer Netherlands, 1999.

[7] J. C. Kasper, M. L. Stevens, A. J. Lazarus, J. T. Steinberg, and K. W. Ogilvie, "Solar wind helium abundance as a function of speed and heliographic latitude: Variation through a solar cycle," *The Astrophysical Journal*, vol. 660, no. 1, pp. 901–910, 2007.

[8] D. M. Hurley, M. Sarantos, C. Grava, *et al.*, "An analytic function of lunar surface temperature for exospheric modeling," *Icarus*, vol. 255, pp. 159–163, 2015.

[9] A. Smolka, *ExESS - extraterrestrial exosphere and surface simulations*, 2023. [Online]. Available: https://smolkaa.github.io.

[10] A. R. Vasavada, J. L. Bandfield, B. T. Greenhagen, *et al.*, "Lunar equatorial surface temperatures and regolith properties from the diviner lunar radiometer experiment," *Journal of Geophysical Research: Planets*, vol. 117, no. E12, n/a–n/a, 2012.

[11] W. F. Huebner and et al., "Solar photo rates for planetary atmospheres and atmospheric pollutants," *Astrophysics and Space Science*, vol. 195, no. 1, pp. 1–294, 1992.

[12] American Meteorological Society, *Glossary of meteorology: Scale height*, 25 April 2012. [Online]. Available: https://glossary.ametsoc.org/wiki/Scale_height.

[13] N. Schörghofer, "Thermodynamics of surface-bounded exospheres," 2020.

[14] J. W. Chamberlain, "Planetary coronae and atmospheric evaporation," *Planetary and Space Science*, vol. 11, no. 8, pp. 901–960, 1963.

[15] N. Schörghofer, "Statistical thermodynamics of surface-bounded exospheres," *Earth, Moon, and Planets*, vol. 126, no. 2, 2022.

[16] C. Lemieux, *Monte Carlo and Quasi-Monte Carlo Sampling*. New York, NY: Springer New York, 2009.

[17] D. J. McComas, M. Bzowski, S. A. Fuselier, *et al.*, "Local interstellar medium: Six years of direct sampling by ibex," *The Astrophysical Journal Supplement Series*, vol. 220, no. 2, pp. 1–11, 2015.

[18] G. Gloeckler and J. Geiss, "Composition of the local interstellar medium as diagnosed with pickup ions," *Advances in Space Research*, vol. 34, no. 1, pp. 53–60, 2004.

[19] J. G. Michels, J. C. Raymond, J. L. Bertaux, *et al.*, "The helium focusing cone of the local interstellar medium close to the sun," *The Astrophysical Journal*, vol. 568, no. 1, pp. 385–395, 2002.

# A Appendix: Supplementary Material
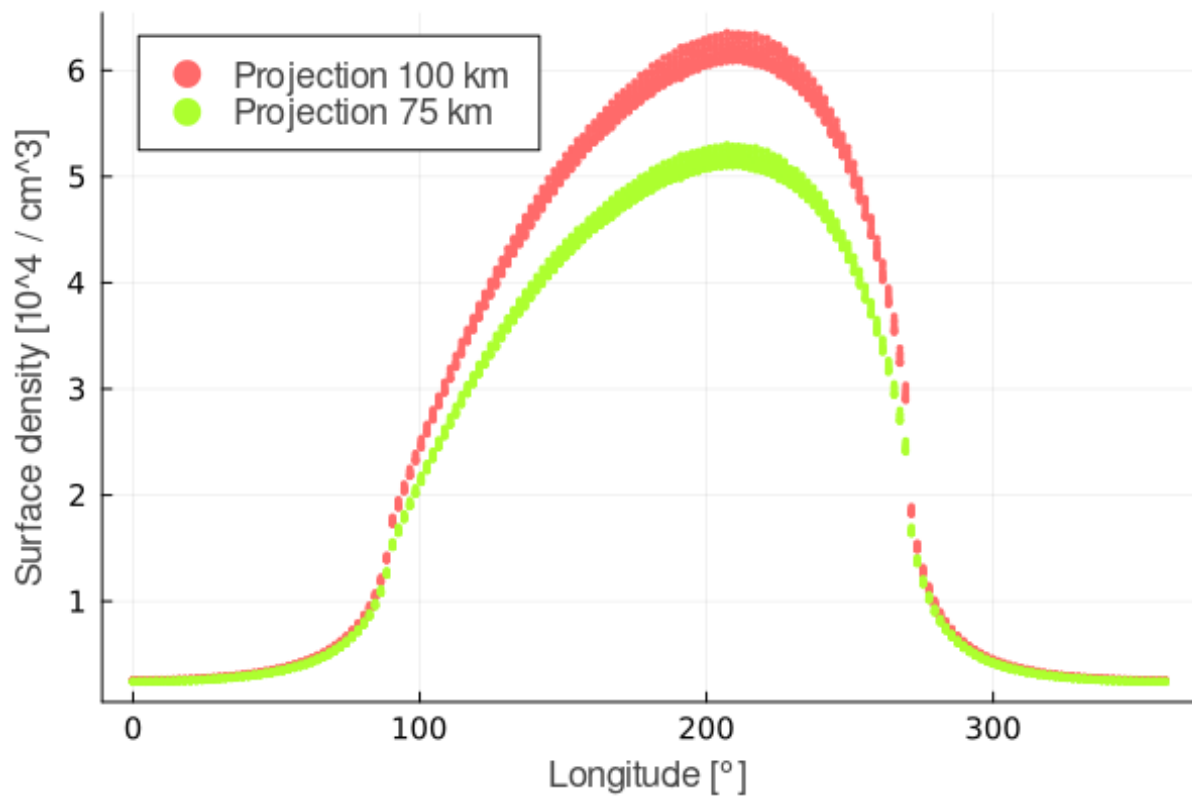
Figure A-1 : *This figure shows layer two's projected surface density data. The data are plotted for the longitudes on the x-axis and with the density on the y-axis. The density development is the same as for layer one and as measured by LADEE. The red data represent the projection from* 100 km *and the greem data from* 75 km.
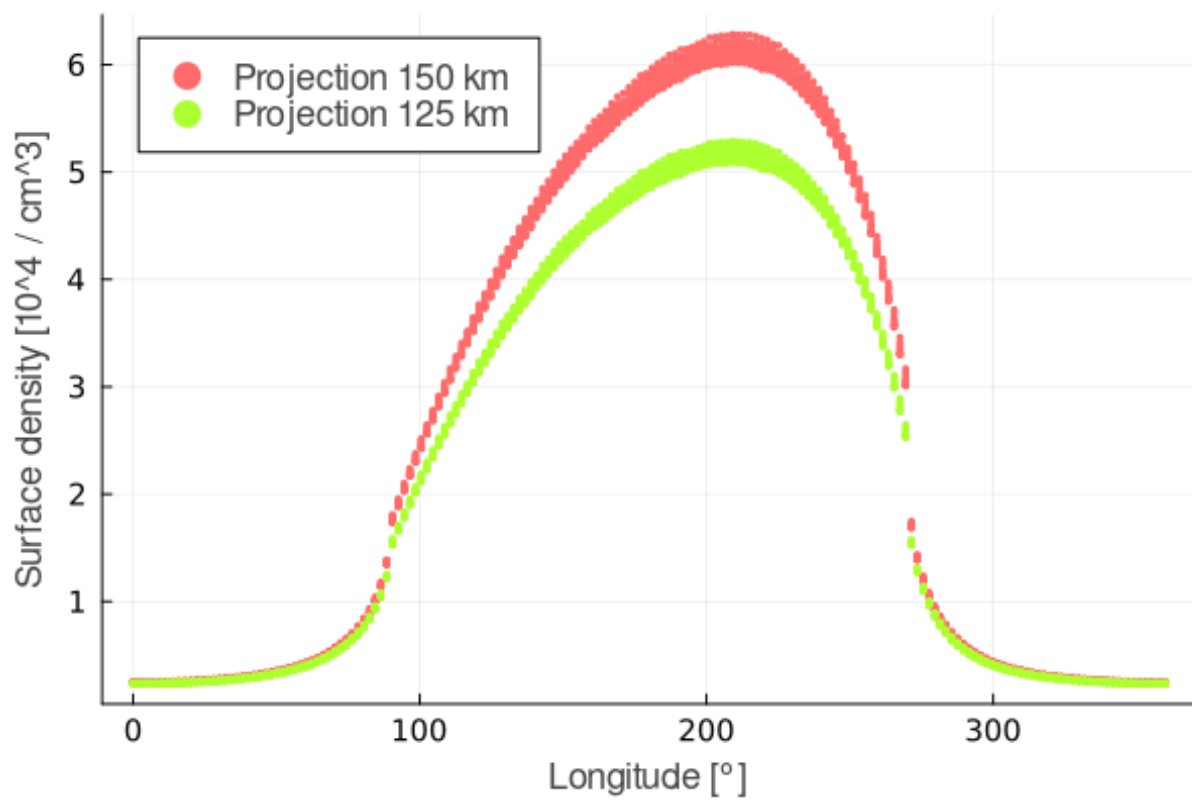
Figure A-2 : This figure shows layer three's projected surface density data. The data are plotted for the longitudes on the x-axis and with the density on the y-axis. The density development is the same as for layer one and as measured by LADEE. The red data represent the projection from $150\ \mathrm{km}$ and the greem data from $125\ \mathrm{km}$.
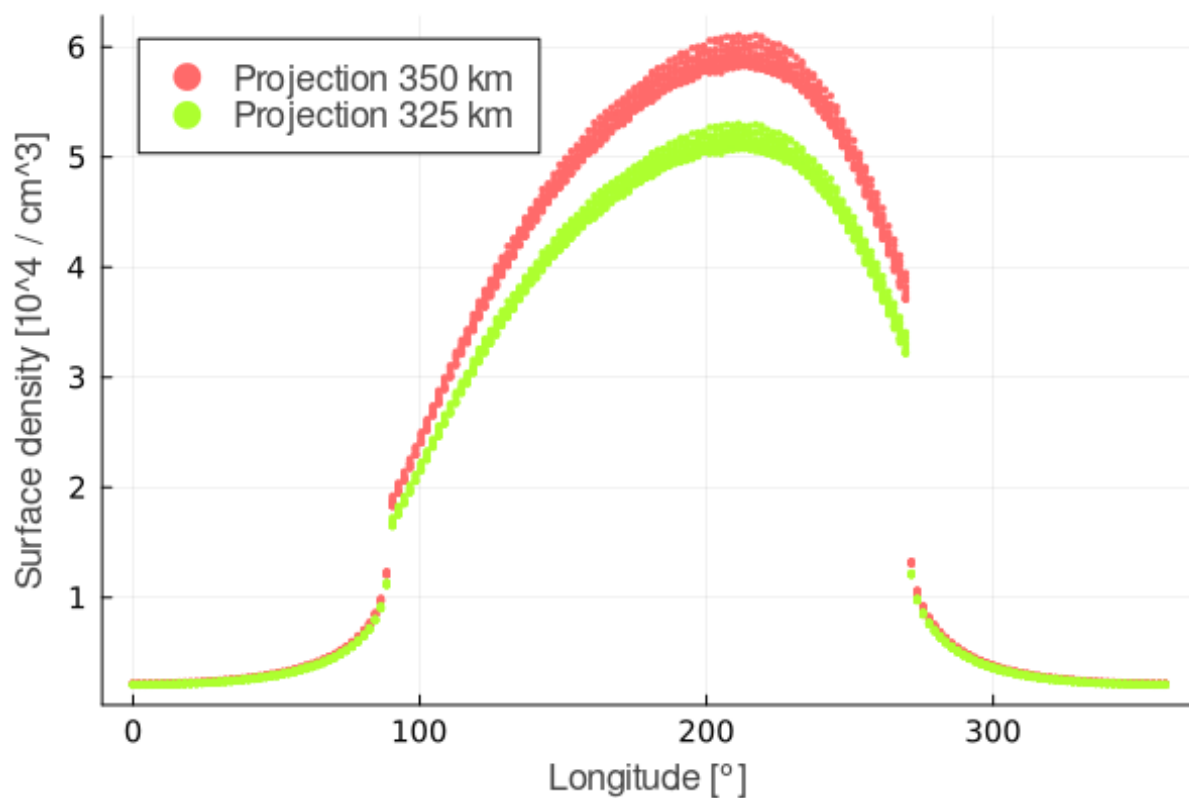
Figure A-3 : This figure shows layer seven's projected surface density data. The data are plotted for the longitudes on the x-axis and with the density on the y-axis. The density development is the same as for layer one and as measured by LADEE. The red data represent the projection from $350\,\mathrm{km}$ and the greem data from $325\,\mathrm{km}$. As presented in chapter 4, the density at the solar sunrise terminator jumps, shown here for layer seven, since the jump is very clearly visible. The reason for the jump is the abrupt temperature difference of the surface, leading to a very different scale height and, therefore, to very different projections of similar densities before and behind the terminator.